Three-body Systems and Kozai-Lidov Oscillations in the Post-Minkowskian Approximation to General Relativity

Zackary A. Windham

A senior thesis submitted to the faculty of
Brigham Young University
in partial fulfillment of the requirements for the degree of

Bachelor of Science

David Neilsen, Advisor

Department of Physics and Astronomy

Brigham Young University

April 2022

ABSTRACT

Three-body Systems and Kozai-Lidov Oscillations in the
Post-Minkowskian Approximation to General Relativity

Zackary A. Windham
Department of Physics and Astronomy, BYU
Bachelor of Science

The Laser Interferometer Gravitational Observatory has detected several large black holes since its launch, leading to an interest in explaining the formation of these massive black holes. We write a code designed to solve N-body gravitational systems with the post-Minkowskian approximation to General Relativity (GR). We use this code to study the Kozai-Lidov mechanism in hierarchical three-body systems. We find that as these hierarchical triple systems move closer together, relativistic effects tend to change the amplitude of Kozai-Lidov oscillations and induce a phase shift between the relativistic oscillations and Newtonian oscillations. Many systems shown to be stable in Newtonian physics flew apart or collided using GR. These findings imply close hierarchical systems can be more unstable in relativistic gravity, which may explain the increased presence of many large black holes.

Keywords: post-Minkowski, general relativity, black holes, Kozai-Lidov, N-body, dynamical capture, post-Newtonian

ACKNOWLEDGMENTS

I am grateful for David Neilsen for guiding and advising me on this project, for him and the College of Physical and Mathematical Sciences at Brigham Young University for providing funding for this project, and for Justin for working alongside me. I am grateful for my family, Ella, and Sasha for supporting me along the way.

Contents

Chapter 1

Introduction

1.1 General Relativity and Black Holes

The beginning physics student will be familiar with Newton's law of gravity, which describes the force of attraction between two bodies with mass. In 1916, Albert Einstein proposed a new mmodel for gravity that accounts for the effects of relativity (Einstein 1916). This new theory of General Relativity (GR) reduces to Newtonian mechanics in the limit of slow moving objects, such that $\frac{v}{c} \ll 1$, and in the limit of a weak gravitational potential, such that $\frac{GM}{rc^2} \ll 1$.

Einstein proposed three tests of GR: measuring the perihelion precession of Mercury's orbit, which precesses more than Newtonian gravity predicts; measuring the deflection of light by the Sun, as GR predicts gravity can bend light; and measuring the gravitational redshift of light (Einstein 1916). Einstein himself conducted the first classical test of GR, showing calculations using GR fully account for the precession of Mercury (Einstein 1916). The deflection of light by the Sun was measured during the total solar eclipse of May 29th, 1919 (Dyson et al. 1920). The gravitational redshift of light from Sirius B was first accurately measured in 1954 (Holberg 2010), fulfilling Einstein's three proposed tests of GR.

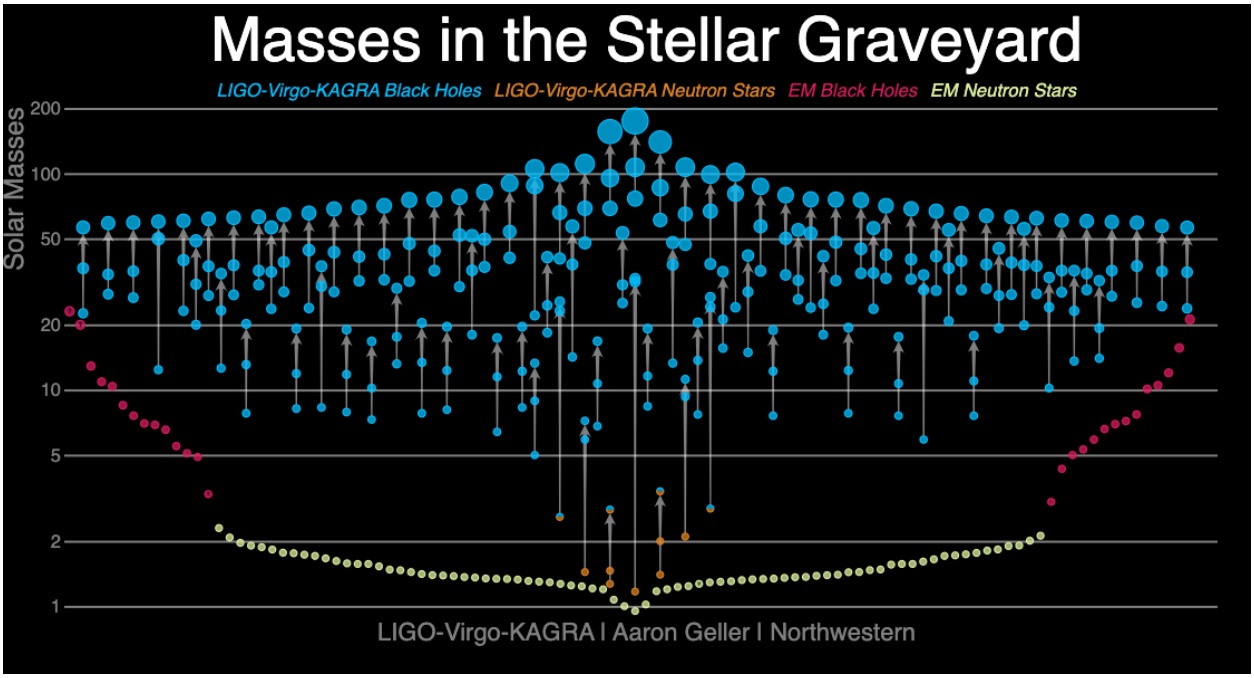

Figure 1.1 A figure depicting the different masses in the stellar graveyard, many detected by LIGO since 2015. The y-axis is in solar masses and the x-axis has no meaning, the masses are simply spread out for organization. Credit: Visualization: LIGO-Virgo-KAGRA / Aaron Geller / Northwestern (Geller 2020)

GR also predicts the existance of black holes, massive objects left behind by dying stars. Stars with masses of about $30\,M_\odot$ or more will collapse to a black hole at the end of its lifespan, as the gravitational contraction will overcome the neutron degeneracy pressure of the core (Oppenheimer & Volkoff 1939). As much of the mass is blown off, a $30\,M_\odot$ star will produce a black hole between $3\,M_\odot$ and $5\,M_\odot$, which is its core mass. Stellar evolution theory predicts that above a certain core mass $M \sim 70\,M_\odot$, a star would violently and completely explode as a pair instability supernova, hence placing an upper limit on the mass of black holes formed through stellar collapse (Woosley & Heger 2021). We do not expect to see many black holes above this upper mass limit in binaries, where they would have formed from stellar evolution.

Massive objects such as black holes can produce gravitational waves through their interactions, another prediction of GR. Recently, gravitational waves have been detected by the Laser Interferom-

eter Gravitational Observatory (LIGO). In 2015 LIGO was able to detect a collision of two black holes (Abbott et al. 2016), and since then has detected many more massive stellar remnants. These findings have populated what we often refer to as the "stellar graveyard", filled with larger mass stellar remnants. LIGO has observed progenitors with masses above $70\,M_{\odot}$, i.e., masses in the mass gap. Multiple mergers of black holes in isolated binaries through gravitational wave emission are expected to be very rare in lifetime of the universe. Another method of forming higher mass black holes is dynamical capture, where the interactions between massive bodies pull a nearby star into a binary or cause an existing binary to collapse.

1.2 The Kozai-Lidov Mechanism

As an example of dynamics processes that can lead to black hole formation through mergers, we study the Kozai-Lidov (KL) mechanism take place. This effect occurs in hierarchical triple systems, where a third body orbits an inner binary. The KL mechanism is characterized by oscillations in the orbital elements of the inner binary, such as the eccentricity and mutual inclination between the two orbital planes (Naoz 2016). These oscillations in the eccentricity of the inner binary can, in particular, accelerate the merger of the inner binary.

Nishizawa et al. (2016) study the formation of black holes in dense star clusters, where dynamical situations are much more common than isolated binaries. They note that binary black hole mergers may be more likely inside the radius of influence of supermassive black holes or in hierarchical triple systems due to the KL mechanism. A higher likelihood of mergers indicates faster creation of black holes with masses above the stellar evolution mass limit. We study hierarchical triple systems with black holes.

1.3 Perturbation Theory

Perturbation theory allows for the approximation of a complex system by perturbing a similar but simpler system. The common perturbative approximation to GR is the post-Newtonian(PN) approximation, which is accurate in the limit that $\left|\frac{GM}{rc^2}\right| \ll 1$ and $\left|\left(\frac{v}{c}\right)^2\right| \ll 1$ (Will 2011). The PN formalism approximates both the potential and the kinetic energy of the system.

A less common approximation is the post-Minkowski(PM) approximation. This approximation treats the kinetic energy exactly and only approximates the gravitational potential, meaning it is accurate always while $\left|\frac{GM}{rc^2}\right| \ll 1$. We use a Hamiltonian that provides the equations of motion for N bodies in the PM approximation (Ledvinka et al. 2008). For a given system, a Hamiltonian $\mathscr{H}$ will give first order differential equations that describe the coordinates q and momenta p of the system. The equations are obtained as $\frac{\partial \mathscr{H}}{\partial p} = \frac{dq}{dt}$ and $\frac{\partial \mathscr{H}}{\partial q} = -\frac{dp}{dt}$. Total time derivatives are denoted as $\frac{dq}{dt} = \dot{q}$.

Suzuki et al. (2020) studied the KL oscillations using the PN approximation and concluded that the oscillations have a significant effect on gravitational wave emission from hierarchical triple systems. They ran different systems using initial conditions for "libration" and "rotation" types. For rotation type initial conditions, the argument of periastron increases monotonically during KL oscillations. For of libration type initial conditions, the argument of periastron oscillates around a specific value during KL oscillations. As the periastron is the point in the orbit where the distance between the two bodies is smallest, this means in rotation type conditions this smallest distance point will move around the orbit of the binary continuously, and in libration type conditions this smallest distance point will oscillate around the same point in space relative to our inertial, center-of-mass reference frame. We study the same systems as Suzuki et al. (2020) using the PM approximation. We decrease the semi-major axes of the systems, however, to enhance relativistic effects, and study how these dynamical systems are affected by relativistic corrections.

Chapter 2

Methods

We solve the PM equations numerically to study hierarchical triple systems of black holes and neutron stars. This section describes our numerical algorithm, and methods for data analysis.

2.1 Differential Equations

Most physics problems involve solving ordinary differential equations (ODEs), whether analytically or numerically. One such system is Newton's equation of gravity, where the acceleration of each body is a function of the distance between the two. As acceleration is the second derivative of distance, this is a differential equation that can be solved to find an expression for the distance as a function of time.

Some ODEs are too complex to be solved analytically and must be solved using numerical approximations. It is important to ensure that the algorithm used to solve the ODEs is accurate. A stable solver will converge to the solution when the step size of approximations is decreased. Decreasing the step size to test the accuracy of the solver is called a convergence test and is vital when using numerical ODE solvers.

2.2 Coding the equations

The PM equations can be written in terms of a Hamiltonian as (Ledvinka et al. 2008)

$$
\begin{aligned}
H = & \sum_a \overline{m}_a - \frac{1}{2} G \sum_{a,b\neq a} \frac{\overline{m}_a \overline{m}_b}{r_{ab}} \left(1 + \frac{p_a^2}{\overline{m}_a^2} + \frac{p_b^2}{\overline{m}_b^2}\right) + \frac{1}{4} G \sum_{a,b\neq a} \frac{1}{r_{ab}} \left(7 \vec{p}_a \cdot \vec{p}_b + (\vec{p}_a \cdot \vec{n}_{ab})(\vec{p}_b \cdot \vec{n}_{ab})\right) \\
& - \frac{1}{4} G \sum_{a,b\neq a} \frac{1}{r_{ab}} \frac{(\overline{m}_a \overline{m}_b)^{-1}}{(y_{ba}+1)^2 y_{ba}} \Big\{ 2 \Big[2 (\vec{p}_a \cdot \vec{p}_b)^2 (\vec{p}_b \cdot \vec{n}_{ba})^2 - 2 (\vec{p}_a \cdot \vec{n}_{ba})(\vec{p}_b \cdot \vec{n}_{ba})(\vec{p}_a \cdot \vec{p}_b) p_b^2 + (\vec{p}_a \cdot \vec{n}_{ba})^2 p_b^4 - (\vec{p}_a \cdot \vec{p}_b)^2 p_b^2 \Big] \frac{1}{\overline{m}_b^2} \\
& + 2 \Big[-p_a^2 (\vec{p}_b \cdot \vec{n}_{ba})^2 + (\vec{p}_a \cdot \vec{n}_{ba})^2 (\vec{p}_b \cdot \vec{n}_{ba})^2 + 2 (\vec{p}_a \cdot \vec{n}_{ba})(\vec{p}_b \cdot \vec{n}_{ba})(\vec{p}_a \cdot \vec{p}_b) + (\vec{p}_a \cdot \vec{p}_b)^2 - (\vec{p}_a \cdot \vec{n}_{ba})^2 p_b^2 \Big] \\
& + \Big[-3 p_a^2 (\vec{p}_b \cdot \vec{n}_{ba})^2 + (\vec{p}_a \cdot \vec{n}_{ba})^2 (\vec{p}_b \cdot \vec{n}_{ba})^2 + 8 (\vec{p}_a \cdot \vec{n}_{ba})(\vec{p}_b \cdot \vec{n}_{ba})(\vec{p}_a \cdot \vec{p}_b) + p_a^2 p_b^2 - 3 (\vec{p}_a \cdot \vec{n}_{ba})^2 p_b^2 \Big] y_{ba} \Big\}
\end{aligned}
\tag{2.1}
$$

Here, $\vec{p}_a$ is the momentum vector of body a. Other quantities are defined as $\overline{m}_a = \sqrt{m_a^2 + p_a^2}$, r_{ab} is the distance between body a and body b, $\vec{n}_{ab} = \frac{\vec{r}_a - \vec{r}_b}{r_{ab}}$ is the unit vector that points from body b to body a, and $y_{ba} = \overline{m}_b^{-1} \sqrt{m_b^2 + (\vec{n}_{ba} \cdot \vec{p}_b)^2}$. The speed of light is set to $c = 1$.

The equations of motion depend on the number of bodies in the system. We use Mathematica to generate the Hamiltonian and analytically derive the equations of motion based on the number of bodies. This script exports the equations of motion as optimized C code and writes the equations to an ASCII file. The equations of motion are then formatted for the Julia (Bezanson et al. 2017) package DIFFERENTIALEQUATIONS.JL(Rackauckas & Nie 2017). We use a Julia script to process the ASCII files and rewrite them as Julia code. The Julia script to solve the equations of motion, called SOLVER.JL, depends on the number of bodies, so this script is automatically generated.

The Julia package DIFFERENTIALEQUATIONS.JL is used to numerically solve the equations of motion. A file containing initial conditions such as the initial positions, initial momenta, masses of the bodies, and the gravitational constant G in code units is fed as an input to the script. The script writes the positions, momenta, and timesteps as a csv output file. The user may choose to solve the system with the Newtonian equations of motion or the PM approximation. In the instance that the bodies are far enough apart, the two sets of equations produce the same results and the Newtonian equations will be much faster. At relativistic speeds and closer distances, the effects of general relativity become important and the PM approximation provides much more accurate results with

regard to GR.

The SOLVER.JL script checks for stopping conditions while solving the equations. Collision detection is done by checking whether horizons of the two bodies overlap. The apparent horizons are approximated as sphere of the Schwarzschild radius. The second stopping condition is triggered when one body has been ejected from the system. This occurs when the separation distances are more than 1000 times the original distances between bodies. At this point, the body is considered to have escaped from the system and any further solution is uninteresting. With these conditions, the code is complete and must be tested to ensure that it produces physical solutions before we can use it solve for systems that exhibit KL oscillations.

2.3 Testing the code

To confirm that the code produces physical solutions, we set initial conditions for a circular binary orbit and ensure the subsequent evolution remains circular. The first-order PM equations do not include the emission of energy from gravitational waves, and so energy is conserved. The condition for circular orbits is that the momentum in the radial direction is zero, and its derivative is zero as well. This derivative indicates that the momentum is entirely tangential, and the radius will never change– hence a circular orbit.

We tried methods from different papers to find the initial conditions for a circular orbit in the PM expansion. Bern et al. (2019) gave a Hamiltonian for the PM expansion in spherical coordinates, which we solved for the initial momentum, setting the radial component of the momentum to zero. The initial momentum given by this formula does not give an exact circular orbit; the orbits are slightly elliptical and precess around each other. Antonelli et al. (2019) states that the Schwarzschild solution should give the correct angular momentum for the circular orbits of two bodies in a first-order PM expansion. Calculating angular momentum from this equation will give imaginary

answers if the bodies are too close, which is when the Schwarzschild solution predicts that the orbit will always be unstable, and the two bodies will crash into each other. However, the solution given by this equation also gives elliptical orbits that precess over time.

Finally, we took the N-body Hamiltonian given by Ledvinka et al. (2008) and substituted in variables in terms of r and θ to transform the equation from Cartesian to spherical coordinates. We set the z components to zero to keep everything in the xy plane and find an expression for the initial angular momentum for a circular orbit (see Appendix A.3). However, this expression cannot be solved analytically and so we used Newton's method to solve for the roots and find the angular momentum. This method of solving for angular momentum proved successful and gives circular orbits. We decreased the step size as well to perform convergence tests and found that the solvers we used converged to the circular solution.

Feng et al. (2018) wrote a PM N-body solver similar to our code. We tested our initial conditions with this code as well, but found that this solver produces results that are much more eccentric and precess at a high rate. We also note that all of the published tests if this code were performed in the Newtonian limit. Due to the inability to produce anything close to circular, we decided this code was not accurate enough to test our results against it.

To choose an integrator for the equations of motion, we test three separate integrators by evolving a binary system with an extremely high eccentricity. Maintaining eccentric orbits for long evolution times is computationally challenging, so the integrator that can last the longest will be the best for evaluating our triple body systems. We test the Vern9 method, the Feagin14 method and a geometric integrator, the TableauExplicitEuler function from Kraus (2020). Vern9 and Feagin14 both have the advantage of using adaptive time steps so that the numerical integration can take smaller steps when needed for convergence. The geometric integrator must use a fixed step, but will conserve certain physical quantities such as the total energy of the system. We use Feagin14 for its high degree of accuracy in integration and computational efficiency (Rackauckas & Nie 2017).

2.4 Deriving initial conditions for runs

We derive the initial conditions for hierarchical three body systems similar to those found in Suzuki et al. (2020), with changes to study relativistic effects in dynamical systems. These initial conditions are given in terms of orbital parameters, however, and must be transformed into Cartesian coordinates for SOLVER.JL. Appendix B1 of Suzuki et al. (2020) gives a process for transforming these orbital parameters into cartesian coordinates for a binary system. We wrote a Julia script that first calculates the initial conditions of the inner binary system, then calculates the initial conditions of a binary system between the third body and the center of mass of the inner binary system. The inner binary coordinates are moved so that we are in the center of mass (COM) frame for the complete system, and our script outputs the initial conditions for all three bodies.

To ensure that our numerical solutions are physical, we monitor some conserved quantities. For example, the total linear momentum should be zero in the center of mass frame. We also calculate the ratio of the momentum of m_3, the outer body orbiting the inner binary, and the Newtonian calculation for what the initial momentum would be for a circle. This was done in the Newtonian limit, and we found the ratio to be approximately one each time.

Because our interest is in relativistic effects, we construct systems at closer distances than those used in Suzuki et al. (2020). Two inequalities must be satisfied for these systems to demonstrate KL behavior. To have a stable hierarchical triple system, we must have

$$\frac{a_{\text{out}}}{a_{\text{in}}} > \frac{2.8}{1-e_{\text{out}}}\left[\left(1+\frac{m_3}{m_{\text{in}}}\right)\frac{1+e_{\text{out}}}{\sqrt{1-e_{\text{out}}}}\right]^{\frac{2}{5}}, \tag{2.2}$$

as given in Mardling & Aarseth (2001). For KL oscillations to occur, we must have

$$\frac{Gm_{\text{in}}}{a_{\text{in}}c^2}\frac{m_{\text{in}}}{m_3}\left(\frac{a_{\text{out}}}{a_{\text{in}}}\right)^3\frac{\left(1-e_{\text{out}}^2\right)^{3/2}}{\left(1-e_{\text{in}}^2\right)^{3/2}} < \frac{3}{4} \tag{2.3}$$

as given by to Suzuki et al. (2020). Solving both of these equations for a_{out} gives us the conditions that must be satisfied for the outer semi-major axis based on the masses of the bodies, eccentricities

PNN		PNB		PNIB		PNSB	
$a_{\rm in}$	$a_{\rm out}$	$a_{\rm in}$	$a_{\rm out}$	$a_{\rm in}$	$a_{\rm out}$	$a_{\rm in}$	$a_{\rm out}$
7.48×10^5 km	$2.463\,18\times10^6$ km	7.48×10^5 km	$5.604\,61\times10^6$ km	7.48×10^5 km	$2.201\,32\times10^7$ km	7.48×10^5 km	$3.484\,95\times10^8$ km
3.74×10^5 km	$1.231\,59\times10^6$ km	3.74×10^5 km	$2.802\,31\times10^6$ km	3.74×10^5 km	$1.100\,66\times10^7$ km	3.74×10^5 km	$1.742\,47\times10^8$ km
1.87×10^5 km	$6.157\,95\times10^5$ km	1.87×10^5 km	$1.401\,15\times10^6$ km	1.87×10^5 km	5.5033×10^6 km	1.87×10^5 km	$8.712\,37\times10^7$ km
9.35×10^4 km	$3.078\,97\times10^5$ km	9.35×10^4 km	$7.005\,77\times10^5$ km	9.35×10^4 km	$2.751\,65\times10^6$ km	9.35×10^4 km	$4.356\,18\times10^7$ km
4.675×10^4 km	$1.539\,49\times10^5$ km	4.675×10^4 km	$3.502\,88\times10^5$ km	4.675×10^4 km	$1.375\,82\times10^6$ km	4.675×10^4 km	$2.178\,09\times10^7$ km
2.3375×10^4 km	$7.697\,43\times10^4$ km	2.3375×10^4 km	$1.751\,44\times10^5$ km	2.3375×10^4 km	$6.879\,12\times10^5$ AU		
$1.168\,75\times10^4$ km	$3.848\,72\times10^4$ km	$1.168\,75\times10^4$ km	$8.757\,21\times10^4$ km	$1.168\,75\times10^4$ km	$3.439\,56\times10^5$ km		
$5.843\,75\times10^3$ km	$1.924\,36\times10^4$ km	$5.843\,75\times10^3$ km	$4.378\,61\times10^4$ km	$5.843\,75\times10^3$ km	$1.719\,78\times10^5$ km		
$2.921\,88\times10^3$ km	$9.621\,79\times10^3$ km	$2.921\,88\times10^3$ km	2.1893×10^4 km	$2.921\,88\times10^3$ km	8.5989×10^4 km		

Table 2.1 Initial semi-major axes for the PNN, PNB, PNIB, and PNSB systems.

of the two orbits, and the semi-major axis of the inner binary.

$$\frac{2.8a_{\rm in}}{1-e_{\rm out}}\left[\left(1+\frac{m_3}{m_{\rm in}}\right)\frac{1+e_{\rm out}}{\sqrt{1-e_{\rm out}}}\right]^{\frac{2}{5}} < a_{\rm out} < \left[\frac{3a_{\rm in}^4 m_3 c^2\left(1-e_{\rm in}^2\right)^{3/2}}{4Gm_{\rm in}^2\left(1-e_{\rm out}^2\right)^{3/2}}\right]^{1/3} \tag{2.4}$$

Suzuki et al. (2020) use nine different three-body systems. In their notation, P stands for a pulsar and N stands for a neutron star, each with a mass of $1.4\,{\rm M}_\odot$. B stands for a black hole with mass $30\,{\rm M}_\odot$, IB stands for an intermediate black hole with mass $1\times10^3\,{\rm M}_\odot$, and SB stands for a supermassive black hole with mass $1\times10^6\,{\rm M}_\odot$. Thus, a PNB system stands for a three-body system where the inner binary is comprised of a pulsar and a neutron star, and the tertiary body is a black hole. The inner binary of each system always contains a pulsar. In Suzuki et al. (2020), the pulsar and neutron star inner binaries are begun with a semi-major axis of 0.01 AU, while the inner binaries comprised of a pulsar and black hole or a pulsar and intermediate-mass black hole begin with a semi-major axis of 0.1 AU. We halve these initial conditions and calculate the smallest possible $a_{\rm out}$ to give the strongest interactions, then halve the systems again until the systems get too close to be stable.

Our code uses units where $\bar{c}=1$, $\bar{G}=1$, and $1\,{\rm M}_\odot=1$, so it is necessary to transform the initial conditions to to this unit system. With units of length L and units of time T, the speed of light in our code units is $c=\bar{c}\frac{L}{T}$, and as $\bar{c}=1$, then $c=\frac{L}{T}$. The units of G gives $G=\bar{G}\frac{L^3}{MT^2}=\bar{G}\frac{Lc^2}{M}$. Solving

PBB		PBIB		PBSB		PIBIB		PIBSB	
a_{in}	a_{out}	a_{in}	a_{out}	a_{in}	a_{out}	a_{in}	a_{out}	a_{in}	a_{out}
7.48×10^6 km	$2.738\,77 \times 10^7$ km	7.48×10^6 km	$8.465\,61 \times 10^7$ km	7.48×10^6 km	$1.325\,24 \times 10^9$ km	7.48×10^6 km	2.7628×10^7 km	7.48×10^6 km	$3.318\,88 \times 10^8$ km
3.74×10^6 km	$1.369\,39 \times 10^7$ km	3.74×10^6 km	4.2328×10^7 km	3.74×10^6 km	$6.626\,18 \times 10^8$ km	3.74×10^6 km	1.3814×10^7 km	3.74×10^6 km	$1.659\,44 \times 10^8$ km
1.87×10^6 km	$6.846\,93 \times 10^6$ km	1.87×10^6 km	2.1164×10^7 km	1.87×10^6 km	$3.313\,09 \times 10^8$ km	1.87×10^6 km	$6.906\,99 \times 10^6$ km	1.87×10^6 km	$8.297\,19 \times 10^7$ km
9.35×10^5 km	$3.423\,47 \times 10^6$ km	9.35×10^5 km	1.0582×10^7 km	9.35×10^5 km	$1.656\,55 \times 10^8$ km	9.35×10^5 km	3.4535×10^6 km	9.35×10^5 km	4.1486×10^7 km
4.675×10^5 km	$1.711\,73 \times 10^6$ AU	4.675×10^5 km	$5.291\,01 \times 10^6$ AU	4.675×10^5 km	$8.282\,73 \times 10^7$ AU			4.675×10^5 km	2.0743×10^7 AU
2.3375×10^5 km	$8.558\,66 \times 10^5$ km	2.3375×10^5 km	2.645×10^6 km	2.3375×10^5 km	$4.141\,36 \times 10^7$ km				
$1.168\,75 \times 10^5$ km	$4.279\,33 \times 10^5$ km	$1.168\,75 \times 10^5$ km	$1.322\,75 \times 10^6$ km	$1.168\,75 \times 10^5$ km	$2.070\,68 \times 10^7$ km				
$5.843\,75 \times 10^4$ km	$2.139\,67 \times 10^5$ km	$5.843\,75 \times 10^4$ km	$6.613\,76 \times 10^5$ km						
$2.921\,88 \times 10^4$ km	$1.069\,83 \times 10^5$ km	$2.921\,88 \times 10^4$ km	$3.306\,88 \times 10^5$ km						

Table 2.2 Initial semi-major axes for the PBB, PBIB, PBSB, PIBIB, and PIBSB systems.

these for length and time units gives the following equations:

$$L = G\frac{M}{c^2} \tag{2.5}$$

$$T = \frac{L}{c} \tag{2.6}$$

Using these values for units of mass, length, and time, we transform the physical initial conditions into unitless variables for the code where $c = 1$ and $G = 1$.

With the initial conditions file, the solver needs to be run for a sufficient length of time to observe KL oscillations. Suzuki et al. (2020) gives the timescale of these oscillations as follows:

$$T_{\text{KL}} \sim \left(\frac{Gm_{\text{in}}}{a_{\text{in}}^3}\right)^{\frac{1}{2}} \frac{a_{\text{out}}^3}{Gm_3}\left(1 - e_{\text{out}}^2\right)^{\frac{3}{2}} \tag{2.7}$$

We run the solver for approximately 15 of these timescales and then store the resulting coordinates and momenta in a csv output file.

Once data are obtained from the runs, it is necessary to transform the coordinates and momenta back into orbital elements to study the KL effect. We follow the procedure described in Appendix B2 of Suzuki et al. (2020). Our method of completing this procedure is described in Appendix A.2 and is written into a Julia script.

Chapter 3

Results and Discussion

3.1 Results

When studying the same systems as Suzuki et al. (2020), we find equivalent results. Oscillations of the inner eccentricity, the inner semimajor axis, and the mutual inclination have similar features in both the Newtonian and the PM runs. Reducing the size of the systems induces a phase shift in the KL oscillations in the relativistic solutions. However, once the bodies get too close to each other the relativistic effects depend heavily on the type of initial conditions used. Figure 3.1 and Figure 3.2 both show the same system, with the only difference being that one system was given rotation type initial conditions and the other was given libration type initial conditions (libration and rotation were described in Section 1.3). Relativistic effects dampen KL oscillations in systems with rotation initial conditions. Relativistic effects amplify the KL oscillations in systems with libration initial conditions. Figure 3.3 shows this amplification effect perhaps most distinctly.

The behavior of the relativistic simulations may be crucial for understanding the dynamical capture in the formation of black holes. Many systems that are stable using Newtonian gravity result in a collision of bodies after several orbits using PM gravity. Figure 3.3 shows massive jumps in

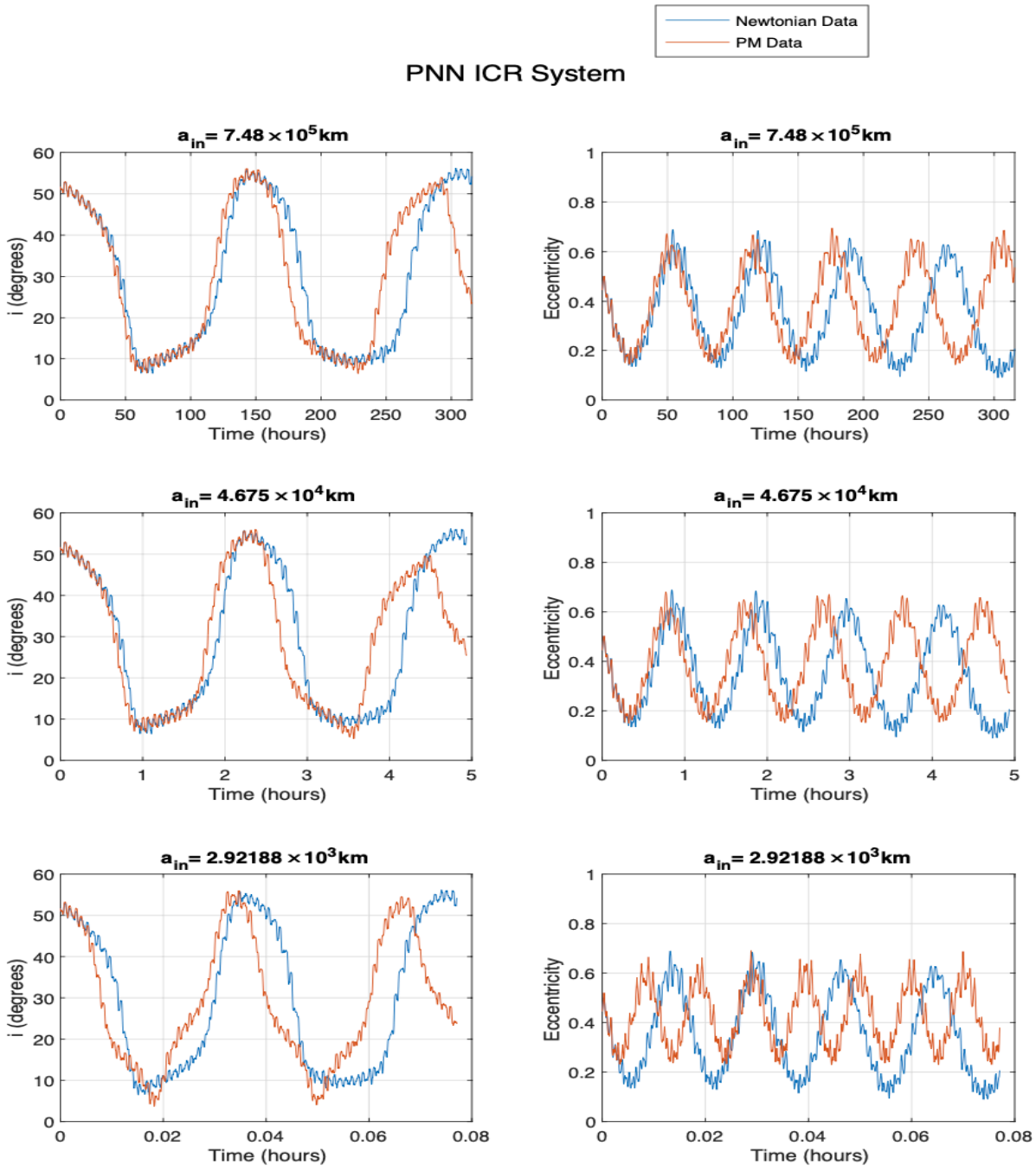

Figure 3.1 Data from an initially circular system with three neutron stars. Initial conditions are of 'rotation' type.

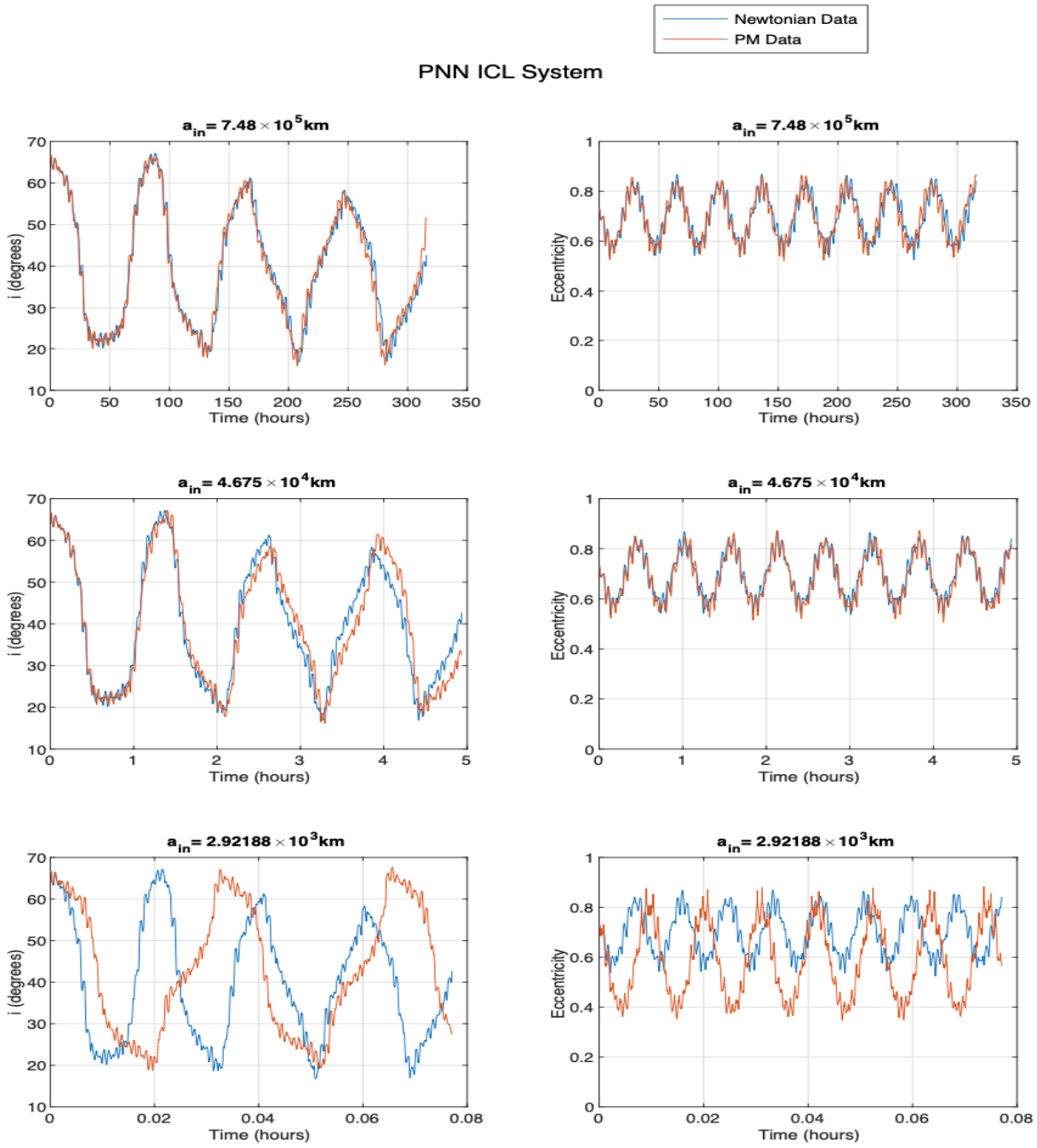

Figure 3.2 Data from an initially circular system with three neutron stars. Initial conditions are of 'libration' type.

eccentricity and mutual inclination between the two orbits. This indicates that smaller hierarchical triple systems are more unstable in relativistic gravity. The collapse of these hierarchical triple systems could be an explanation for the presence of more large black holes.

3.2 Future Research

While this work presents some initial results of multi-body PM systems, further research is needed to understand the full range of possible relativistic effects in multi-body systems. A study with higher order equations would be able to determine the nature of hierarchical triple systems in relativistic gravity with greater accuracy and better establish whether they allow for a high degree of dynamical capture. Calculating the velocity at periapsis for each orbit would help determine if second order terms are necessary; if the velocity is near $0.1c$ then it is likely the approximation is not accurate without second order terms. Comparing these results to those found using second order PN equations would also be an enlightening way to check accuracy. Modifying the code to track the value of the Hamiltonian as well as the value of $\left|\frac{GM}{rc^2}\right|$ would help to check the physicality of our results, as the Hamiltonian should not change and the value of $\left|\frac{GM}{rc^2}\right|$ should stay much smaller than 1.

Suzuki et al. (2020) mention the Lense-Thirring precession effect, a spin-orbit coupling effect introduced in 1.5 PN order simulations. In order to avoid this effect they keep their systems relatively large, so that they can be certain all effects in their data are from the Kozai-Lidov effect. It would be of interest to find if a similar effect exists in the PM approximation and if this effect could be producing some of results seen in the data from our smaller systems.

The code developed for this study could be used to study larger systems as well, such as small clusters. Though these simulations would be computationally expensive, the behavior of these systems in relativistic gravity could provide useful insights into the possibility of dynamical capture

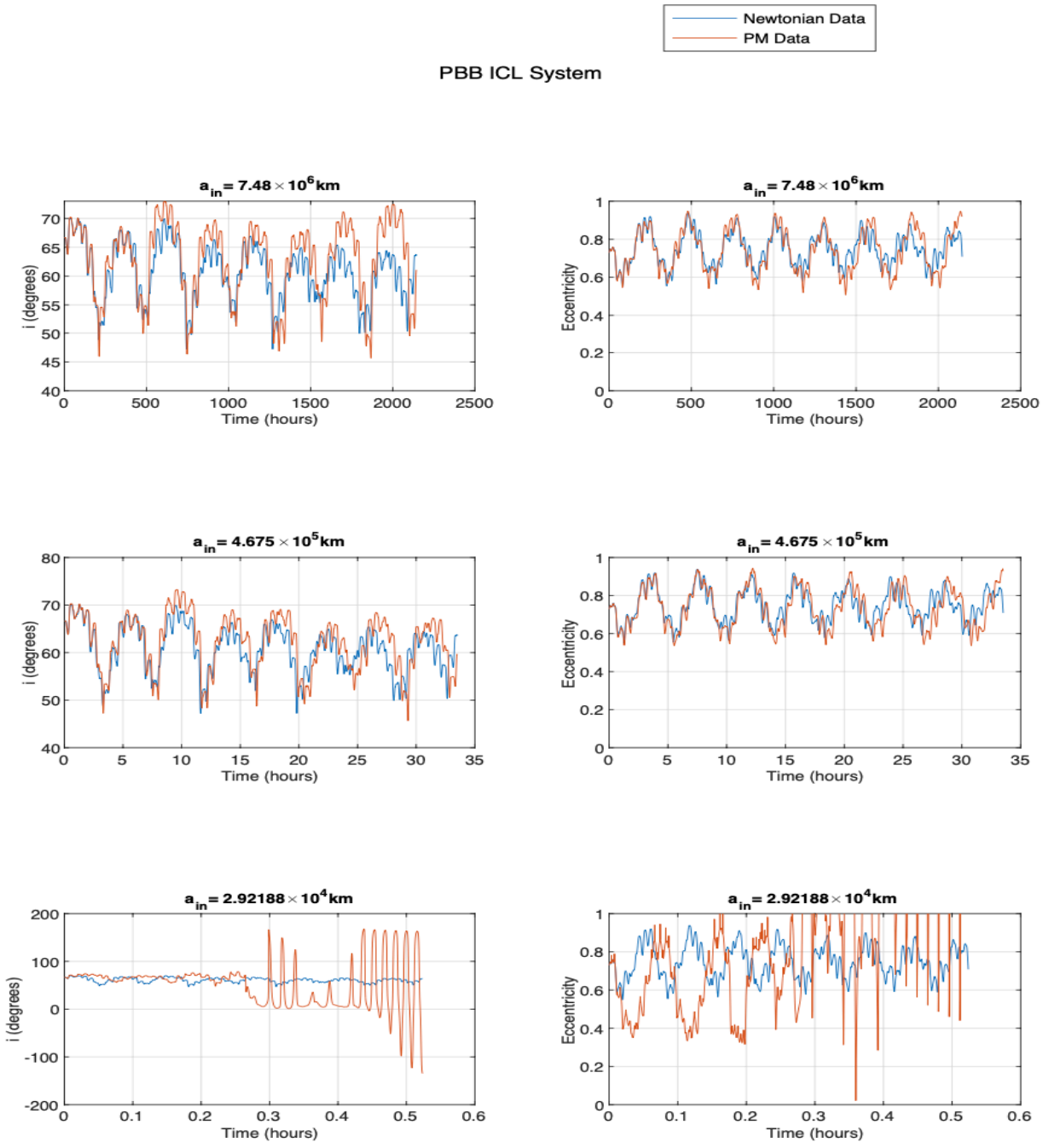

Figure 3.3 Data from an initially circular system with a neutron star and two black holes. Initial conditions are of 'libration' type.

as well. A recent paper, Zwart et al. (2021), studied the chaotic nature of many body systems in PN gravity. A comparison of similar systems computer with PM gravity could be interesting.

Appendix A

Derivations

A collection of derivations for different processes used throughout the paper.

A.1 Transformation to Cartesian coordinates

We use the same methods for transferring between Cartesian coordinates and orbital elements as Suzuki et al. (2020). Beginning with initial orbital elements, the semi-major axis a, eccentricity e, inclination i, argument of periastron ω, longitude of ascending node Ω, and mean anomaly $\mathscr{M}$. The eccentric anomaly u and true anomaly f are found using the following equations:

$$\mathscr{M} = u - e\sin u \tag{A.1}$$

$$f = \arctan\left[\frac{(\sin u)\sqrt{1-e^2}}{\cos u - e}\right] \tag{A.2}$$

From this we can find polar coordinates as follows:

$$r = \frac{a\left(1-e^2\right)}{1-e\cos f} \tag{A.3}$$

$$\phi = \Omega + \arctan\left[\tan\left(\omega + f\right)\cos i\right] \tag{A.4}$$

$$\theta = \arccos\left[\sin\left(\omega + f\right)\sin i\right] \tag{A.5}$$

For calculating initial conditions we must also have initial velocity and momenta. This is done as follows:

$$\dot{r} = g_r \dot{f} \tag{A.6}$$

$$\dot{\theta} = g_\theta \dot{f} \tag{A.7}$$

$$\dot{\phi} = g_\phi \dot{f} \tag{A.8}$$

with

$$g_r = \frac{a\left(1-e^2\right) e \sin f}{\left(1+e\cos f\right)^2} \tag{A.9}$$

$$g_\theta = -\frac{1}{\sin\theta}\cos\left(\omega+f\right)\sin i \tag{A.10}$$

$$g_\phi = \cos^2\left(\phi+\Omega\right)\frac{\cos i}{\cos^2\left(\omega+f\right)} \tag{A.11}$$

$$\dot{f} = \sqrt{GM\left(\frac{2}{r}-\frac{1}{a}\right)\frac{1}{g_r^2+\left(rg_\theta\right)^2+\left(r\sin\theta g_\phi\right)^2}} \tag{A.12}$$

Here, $M = m_1 + m_2$ being the total mass of the two bodies in the binary. From this point, Cartesian coordinates and momenta are calculated as follows:

$$x = r\sin\theta\cos\phi \tag{A.13}$$

$$y = r\sin\theta\sin\phi \tag{A.14}$$

$$z = r\cos\theta \tag{A.15}$$

$$\dot{x} = \dot{r}\sin\theta\cos\phi + r\dot{\theta}\cos\theta\cos\phi - r\dot{\phi}\sin\theta\sin\phi \tag{A.16}$$

$$\dot{y} = \dot{r}\sin\theta\sin\phi + r\dot{\theta}\cos\theta\sin\phi + r\dot{\phi}\sin\theta\cos\phi \tag{A.17}$$

$$\dot{z} = \dot{r}\cos\theta - r\dot{\theta}\sin\theta \tag{A.18}$$

Defining vectors $\vec{q} = (x,y,z)$ and $\vec{v} = (\dot{x},\dot{y},\dot{z})$, with $\vec{q}_1$ and $\vec{p}_1$ as the position and momentum vectors of the body with mass m_1, $\vec{q}_2$ and $\vec{p}_2$ as the position and momentum vectors of the body with mass m_2, and $\mu = \frac{m_1 m_2}{M}$, we have the following expressions for these vectors:

$$\vec{q}_1 = \frac{m_2}{M}\vec{q} \tag{A.19}$$

$$\vec{q}_2 = -\frac{m_1}{M}\vec{q} \tag{A.20}$$

$$\vec{p}_1 = \mu\vec{v} \tag{A.21}$$

$$\vec{p}_2 = -\mu\vec{v} \tag{A.22}$$

For hierarchical triple systems, the initial conditions for the two binaries (the inner binary of two masses and the outer binary of the third mass and the center of mass of the inner binary) are calculated separately and then moved to be in the center of mass frame for the entire system.

A.2 Transformation to orbital elements

In order to analyze the data from runs, the Cartesian coordinates for position and momenta that are output must be transformed back into orbital elements. Firstly, with $M = m_1 + m_2$ and $\mu = \frac{m_1 m_2}{M}$, we begin with $\vec{q}$ and $\vec{p}$ for each body, the coordinates and momenta output by the code. We define the following vectors:

$$\dot{\vec{q}}_1 = \frac{\vec{p}_1}{m_1} \tag{A.23}$$

$$\dot{\vec{q}}_2 = \frac{\vec{p}_2}{m_2} \tag{A.24}$$

Here it is essential to remember to move the inner binary out of the center of mass frame of the whole system when calculating its orbital elements, and thus calculate the speeds in the reference frame of the center of mass of only this binary. We then define the following new vectors, remembering that for the outer binary $\vec{q}_2$ lies at the center of mass of the inner binary:

$$\vec{r} = \vec{q}_1 - \vec{q}_2 \tag{A.25}$$

$$\vec{v} = \dot{\vec{r}} = \frac{\vec{p}_1}{\mu} \tag{A.26}$$

From this point, we define the energy per unit mass of the system as follows:

$$E = \frac{1}{2}v^2 - \frac{GM}{r} \tag{A.27}$$

At this point we may derive four of the orbital elements, as follows:

$$a = -\frac{GM}{2E} \tag{A.28}$$

$$i = \arccos\left[\frac{(\vec{r}\times\vec{v})_z}{|\vec{r}\times\vec{v}|}\right] \tag{A.29}$$

$$e = \sqrt{1 - \frac{|\vec{r}\times\vec{v}|^2}{aGM}} \tag{A.30}$$

$$\Omega = \arccos\left[\frac{(\hat{z}\times(\vec{r}\times\vec{v}))_x}{|\hat{z}\times(\vec{r}\times\vec{v})|}\right] \tag{A.31}$$

We now have the semimajor axis a, the inclination i, the eccentricity e, and the longitude of the ascending node Ω. Two additional quantities must be derived to give the argument of periastron: the true anomaly f and the angle from the ascending node θ:

$$f = \arccos\left[\frac{a\left(1-e^2\right)-r}{er}\right] \tag{A.32}$$

$$\theta = \arccos\left(\frac{x\cos\Omega + y\sin\Omega}{r}\right) \tag{A.33}$$

where $x = \vec{r}_x$ and $y = \vec{r}_y$. The argument of periastron is then easily obtained as follows:

$$\omega = \theta - f \tag{A.34}$$

A.3 Circular Initial Conditions

Mathematically a circular orbit can be defined as a system where

$$\dot{p}_\theta = 0, \tag{A.35}$$

with p_θ as the momentum tangential to the direction of motion. p_r, momentum in the radial direction, will be zero as there is no motion in the radial direction. Equation A.35 corresponds to

the conservation of angular momentum. In order to solve for this, we took equation 2.1 and took the derivative with respect to r, giving

$$\dot{p}_\theta = -\frac{\partial H}{\partial r} \tag{A.36}$$

This equation is then set equal to 0 and solved for p_θ, the initial angular momentum for a circle. The resulting equation cannot be solved analytically, so we implemented Newton's method to solve for the correct initial angular momentum for each individual system based on the masses of the bodies and the distance between them.

Appendix B

Additional Figures

This is appendix is comprised of figures and data from other runs.

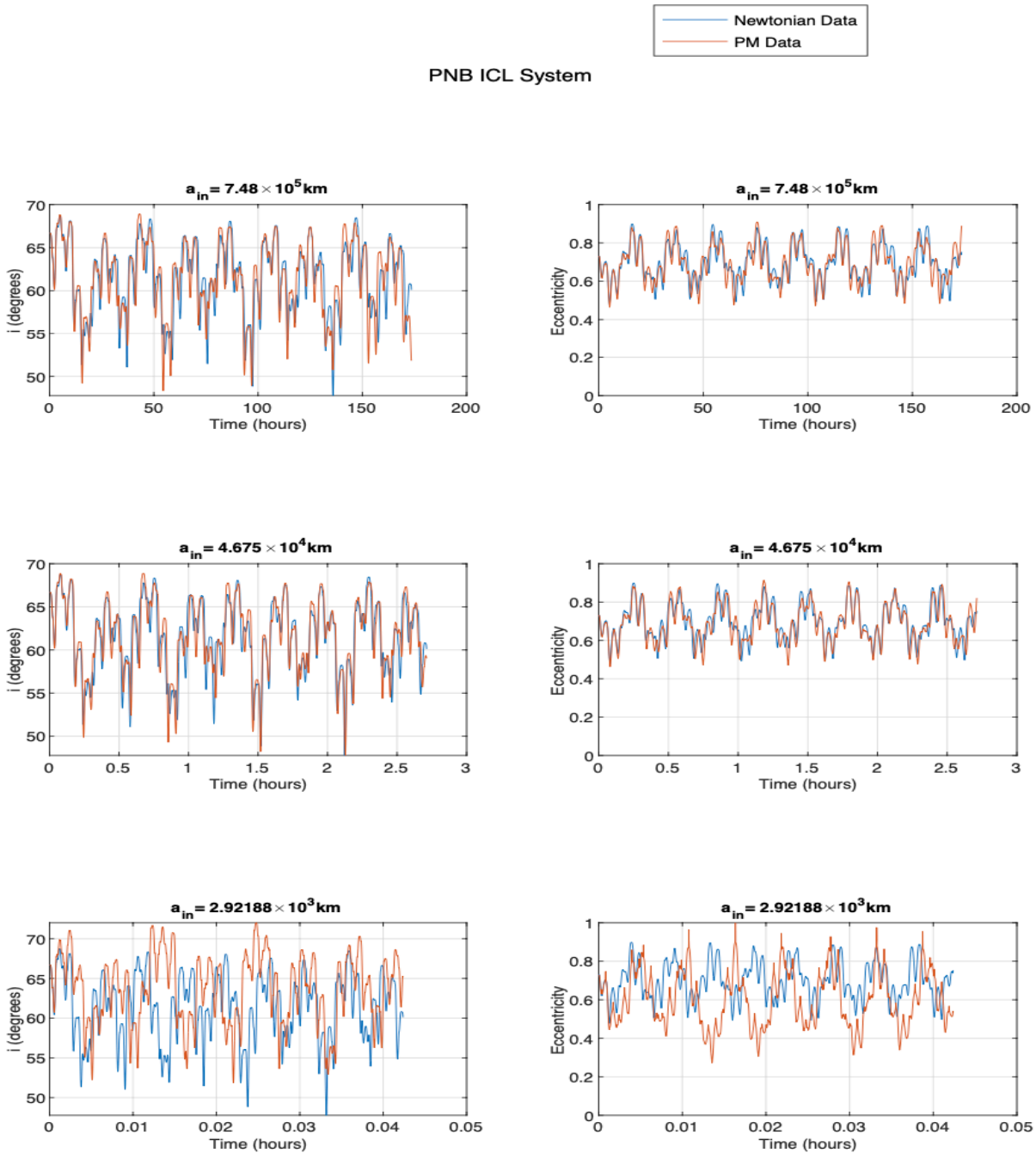

Figure B.1 Data from an initially circular system with two neutron stars and a black hole. Initial conditions are of 'libration' type.

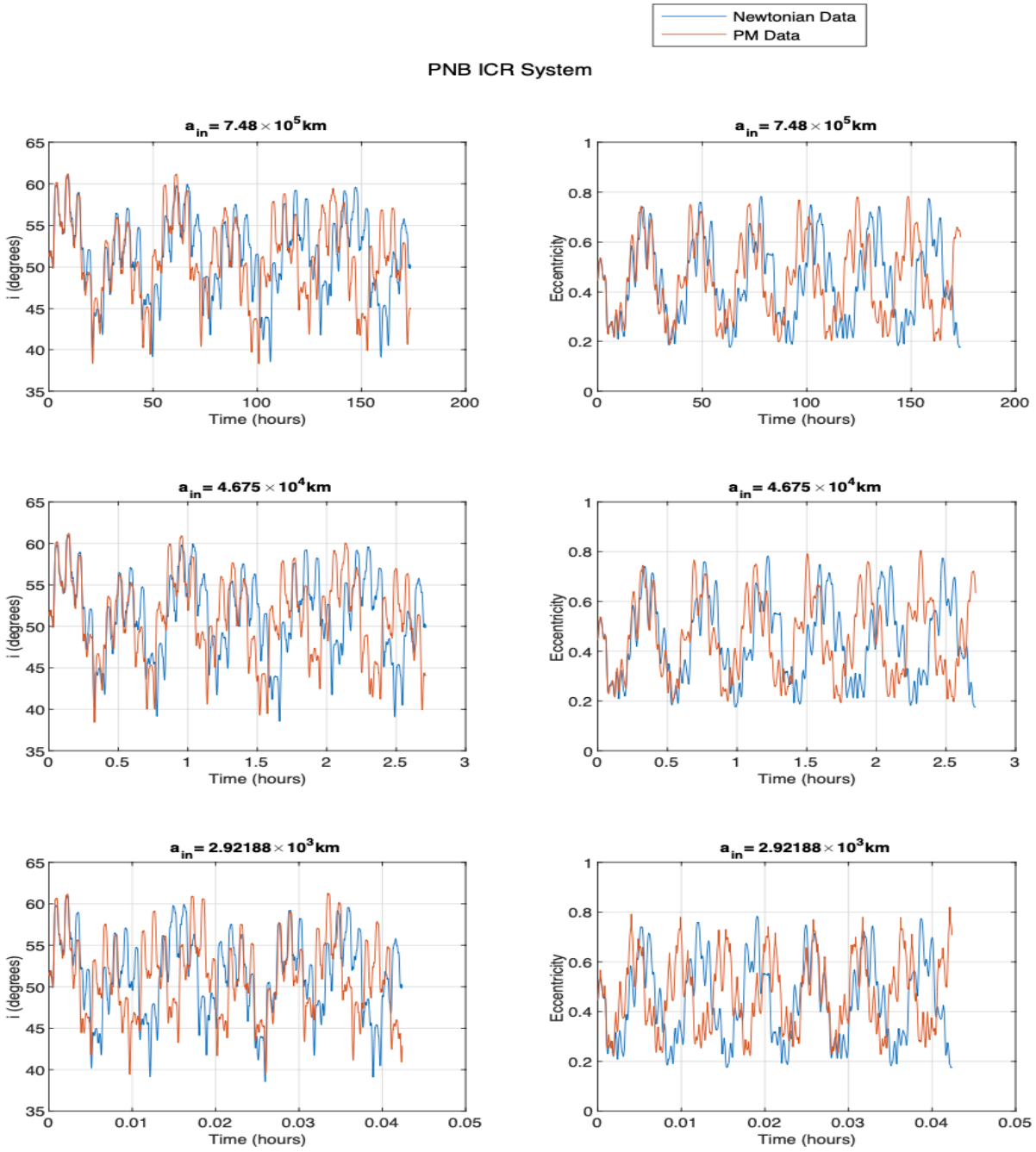

Figure B.2 Data from an initially circular system with two neutron stars and a black hole. Initial conditions are of 'rotation' type.

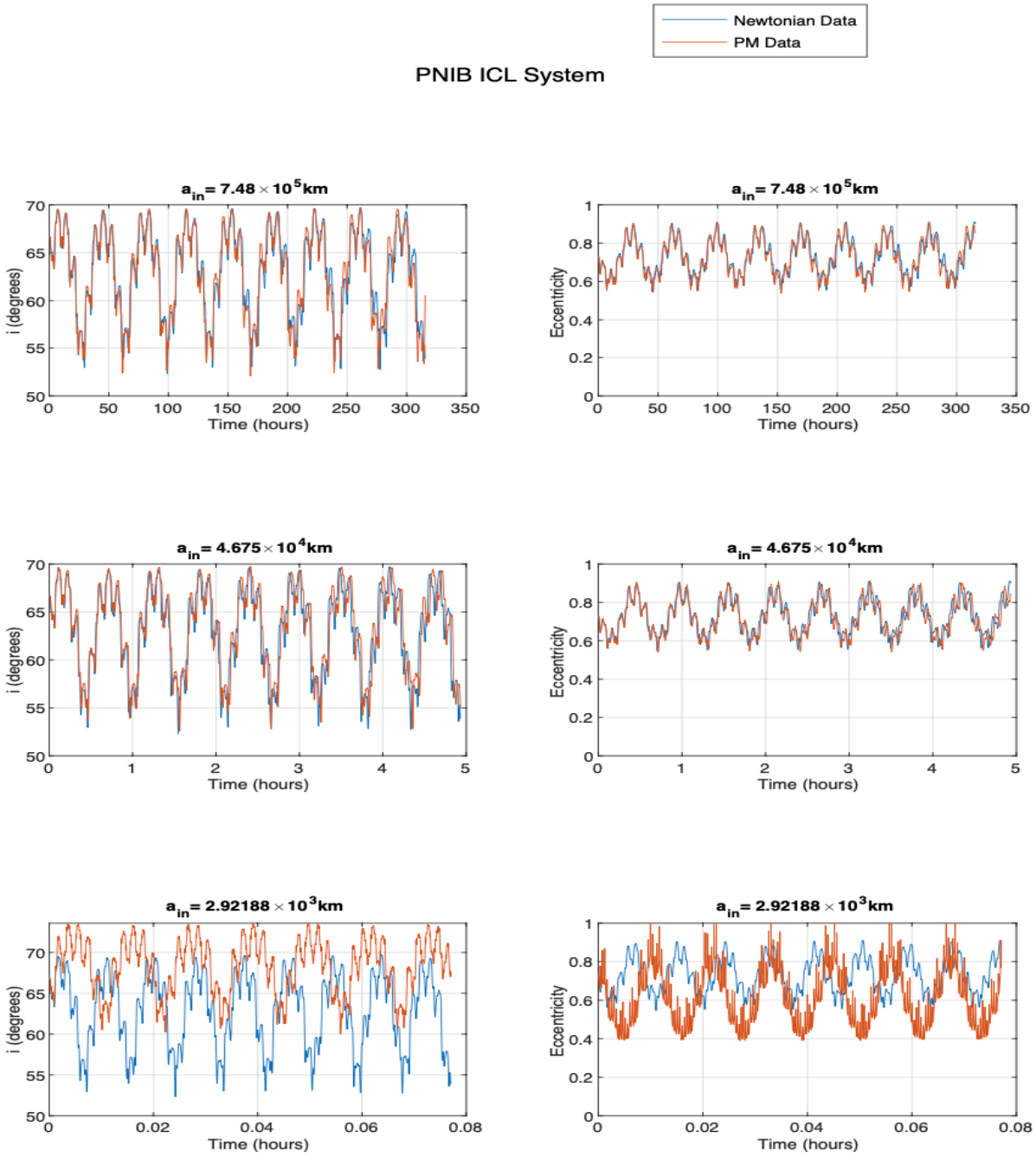

Figure B.3 Data from an initially circular system with two neutron stars and an intermediate mass black hole. Initial conditions are of 'libration' type.

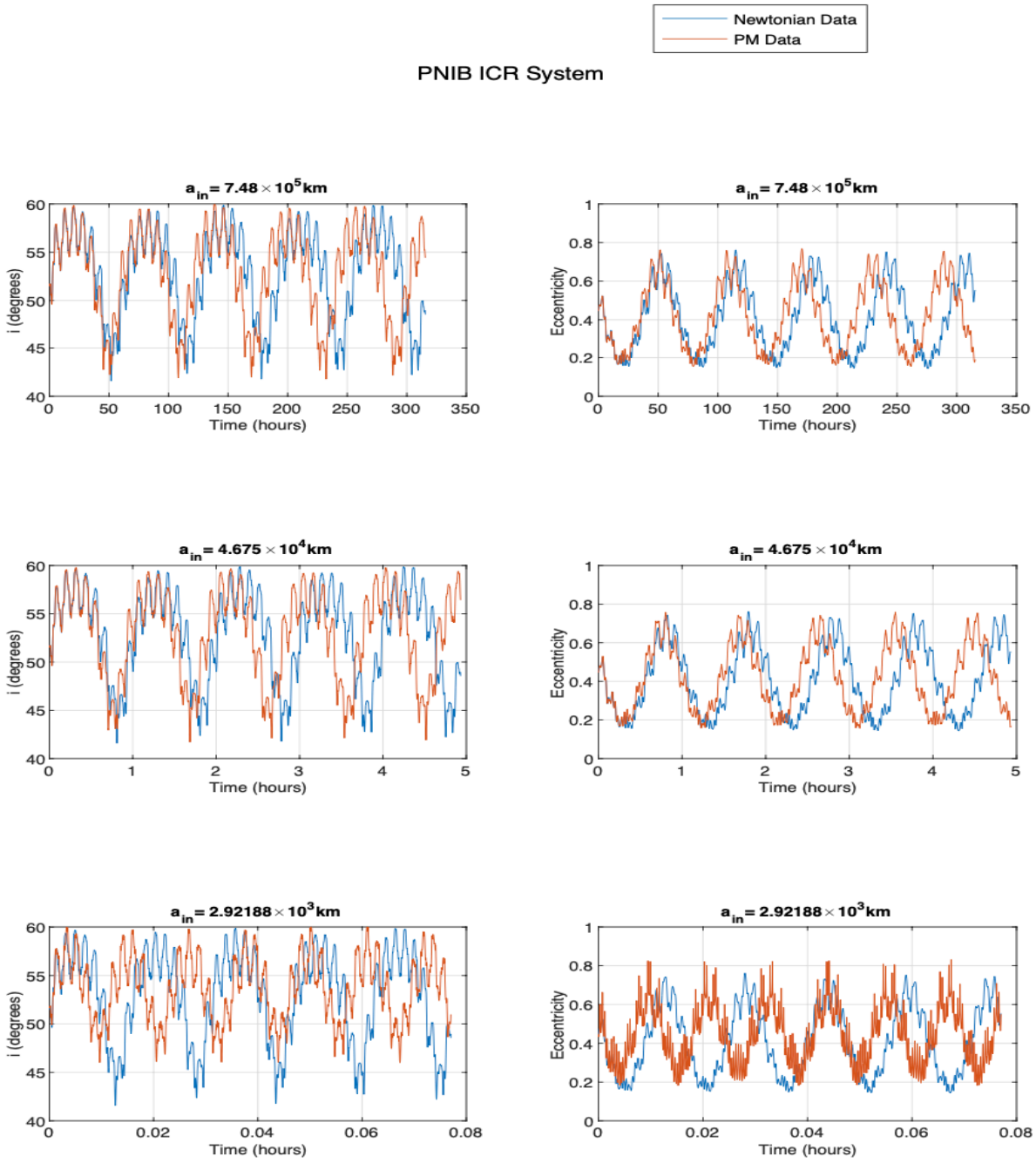

Figure B.4 Data from an initially circular system with two neutron stars and an intermediate mass black hole. Initial conditions are of 'rotation' type.

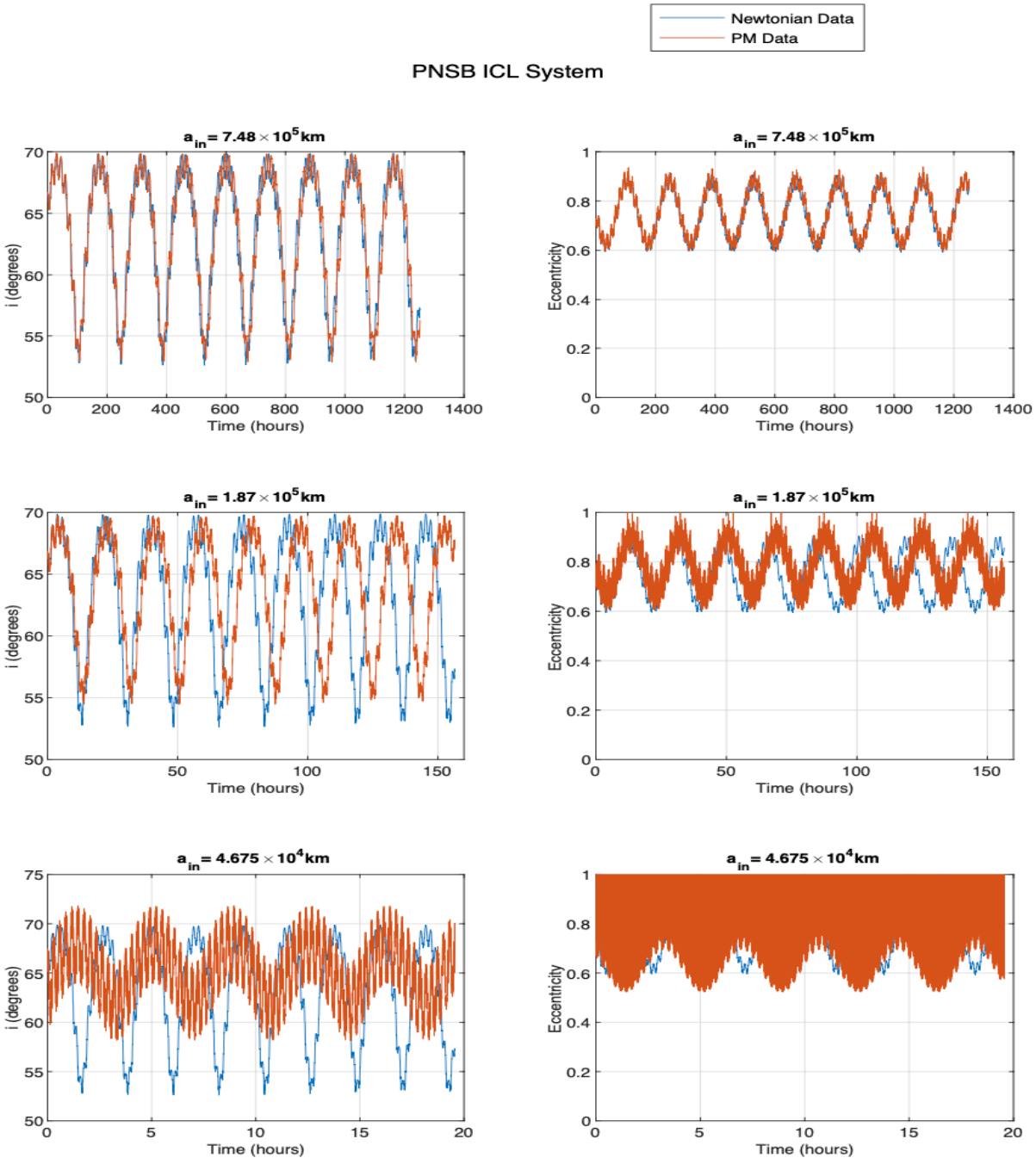

Figure B.5 Data from an initially circular system with two neutron stars and an super-massive black hole. Initial conditions are of 'libration' type.

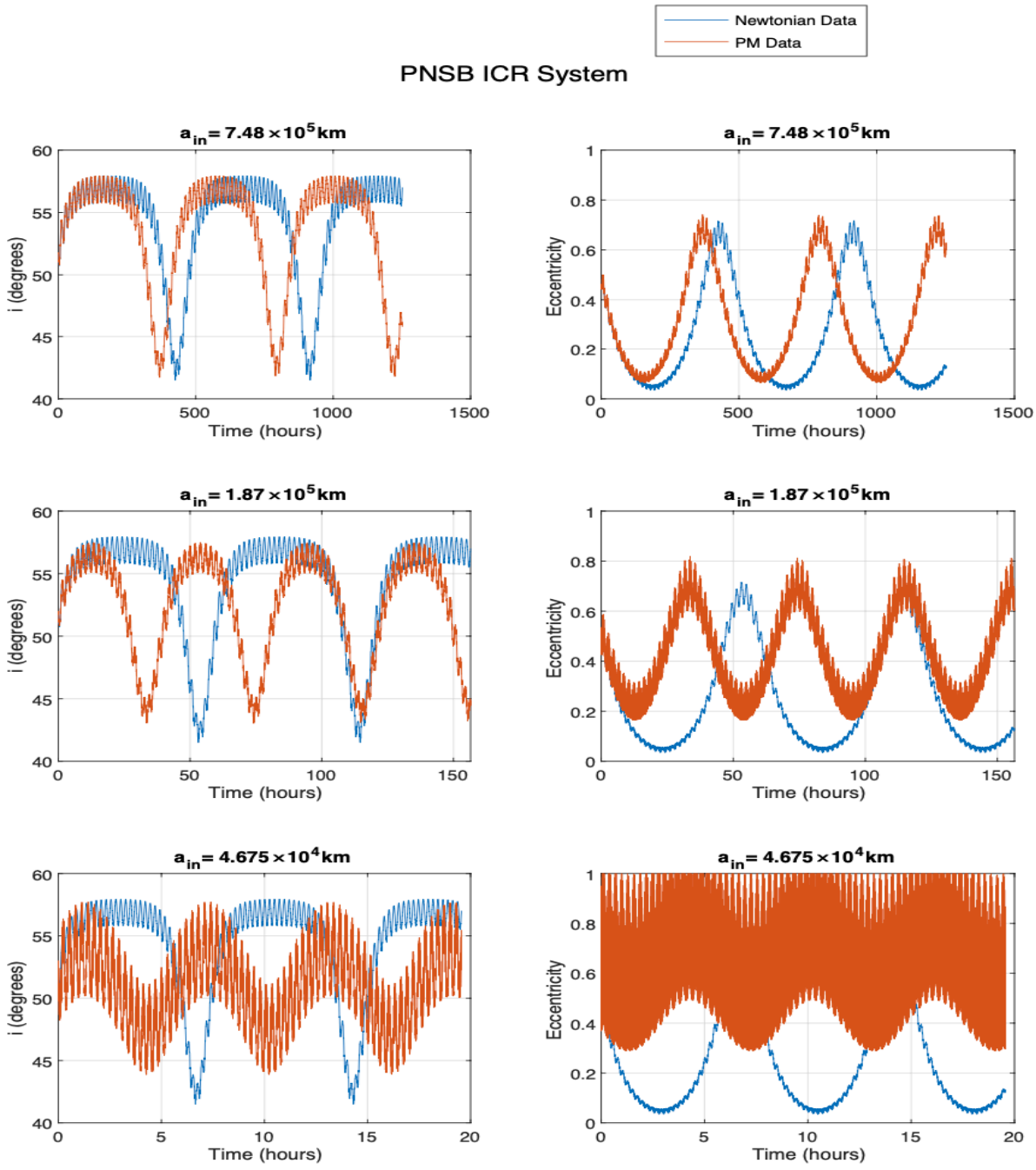

Figure B.6 Data from an initially circular system with two neutron stars and a supermassive black hole. Initial conditions are of 'rotation' type.

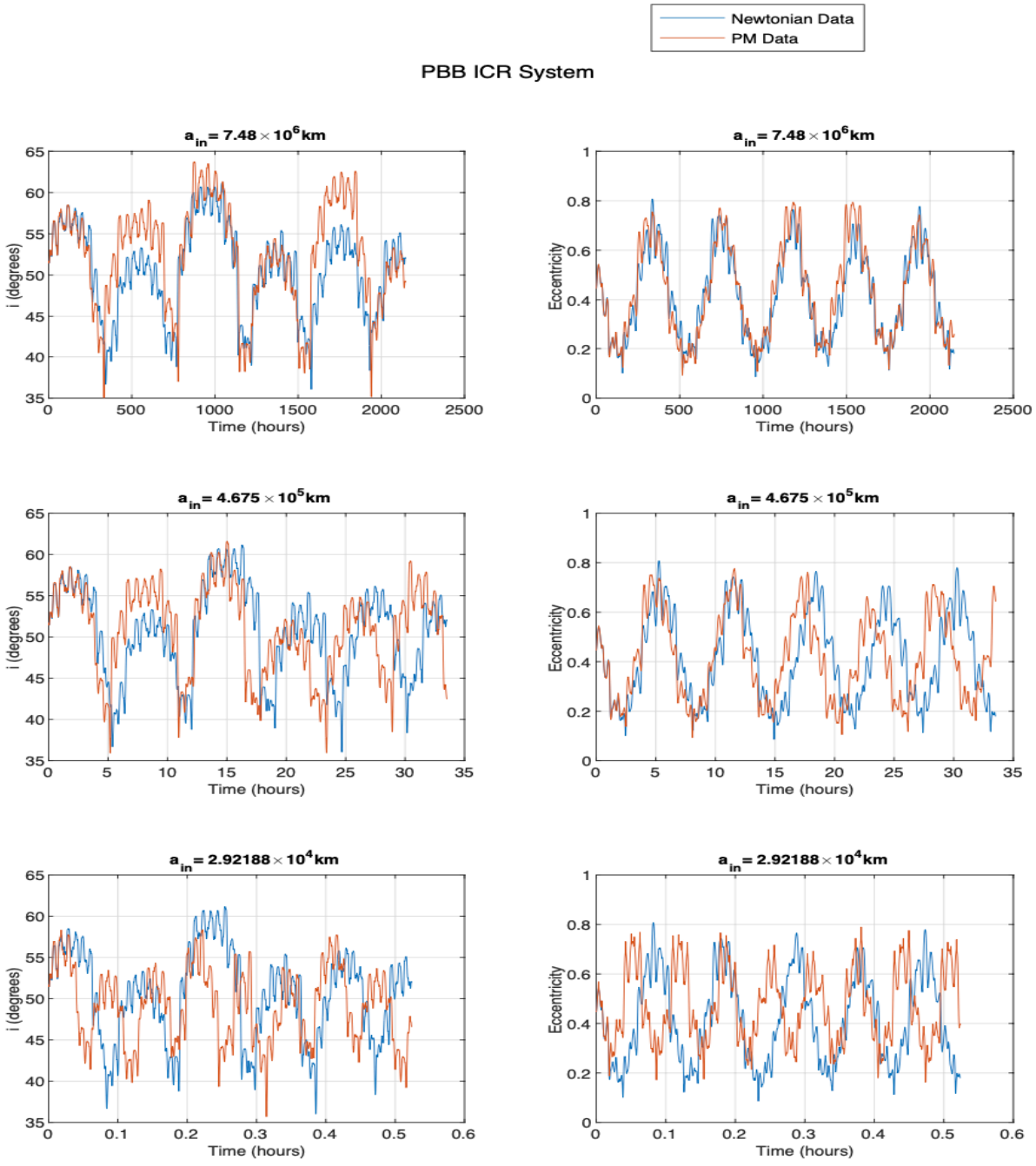

Figure B.7 Data from an initially circular system with a neutron star and two black holes. Initial conditions are of 'rotation' type.

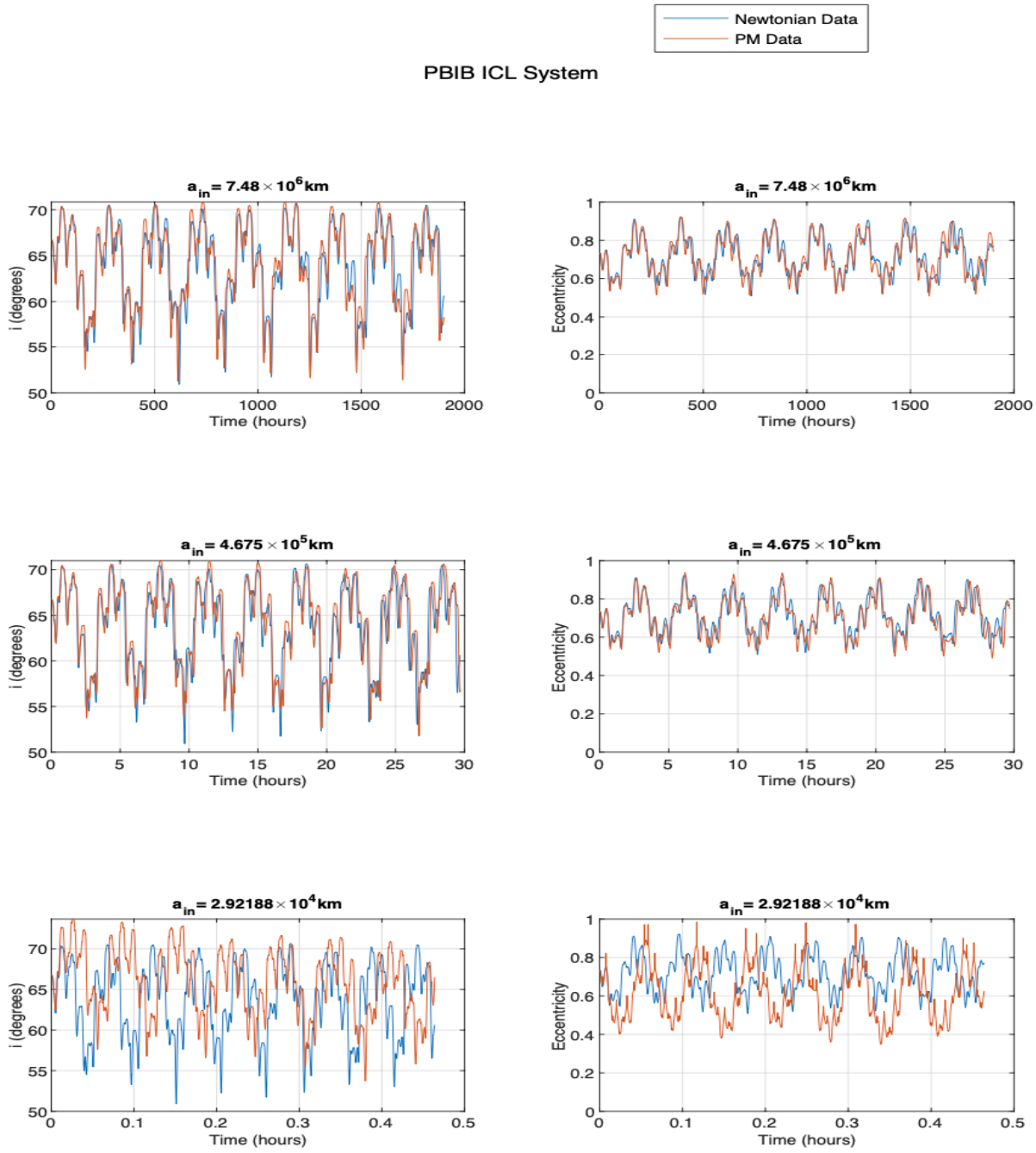

Figure B.8 Data from an initially circular system with a neutron star, a black hole, and an intermediate mass black hole. Initial conditions are of 'libration' type.

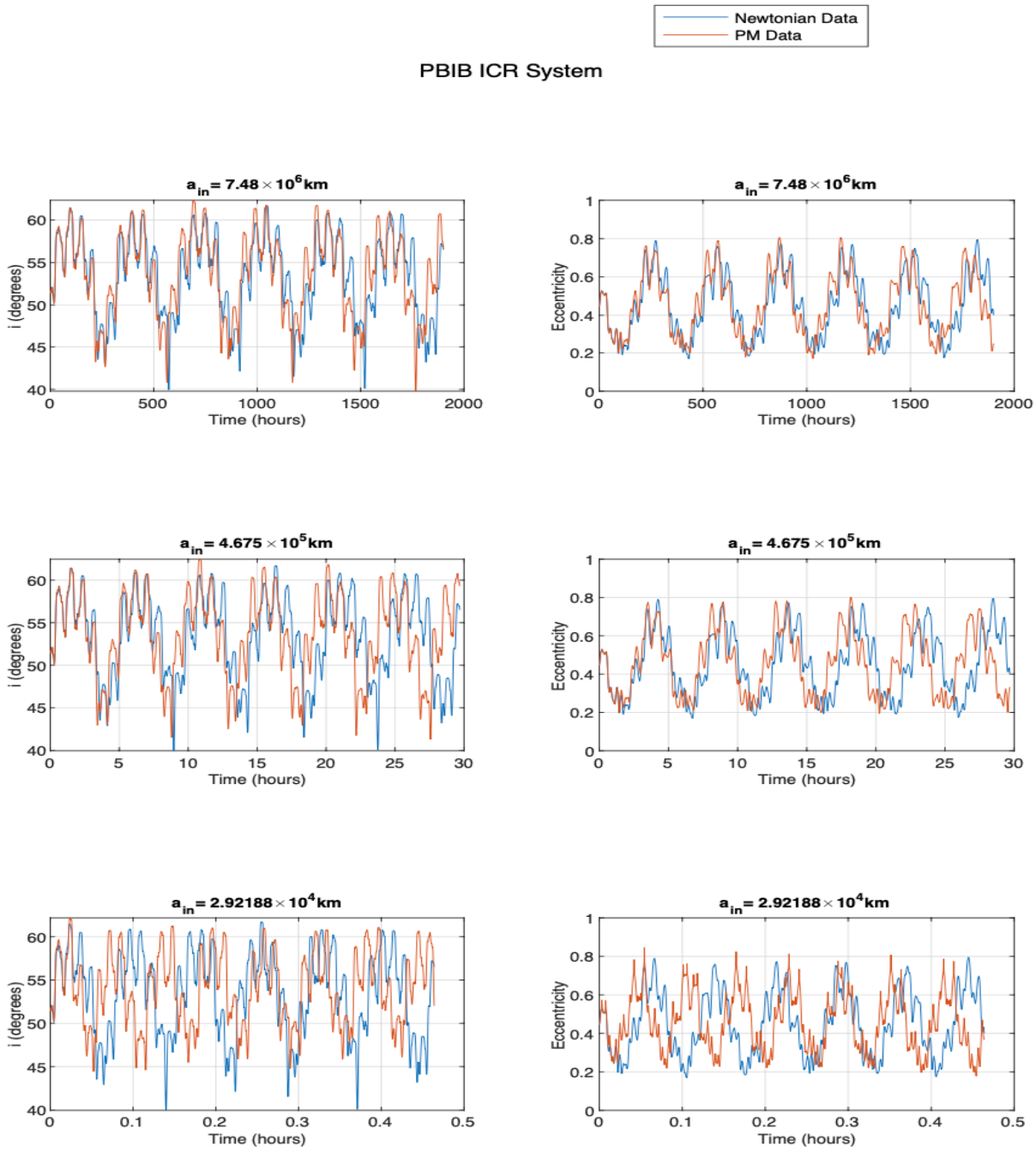

Figure B.9 Data from an initially circular system with a neutron star, a black hole, and an intermediate mass black hole. Initial conditions are of 'rotation' type.

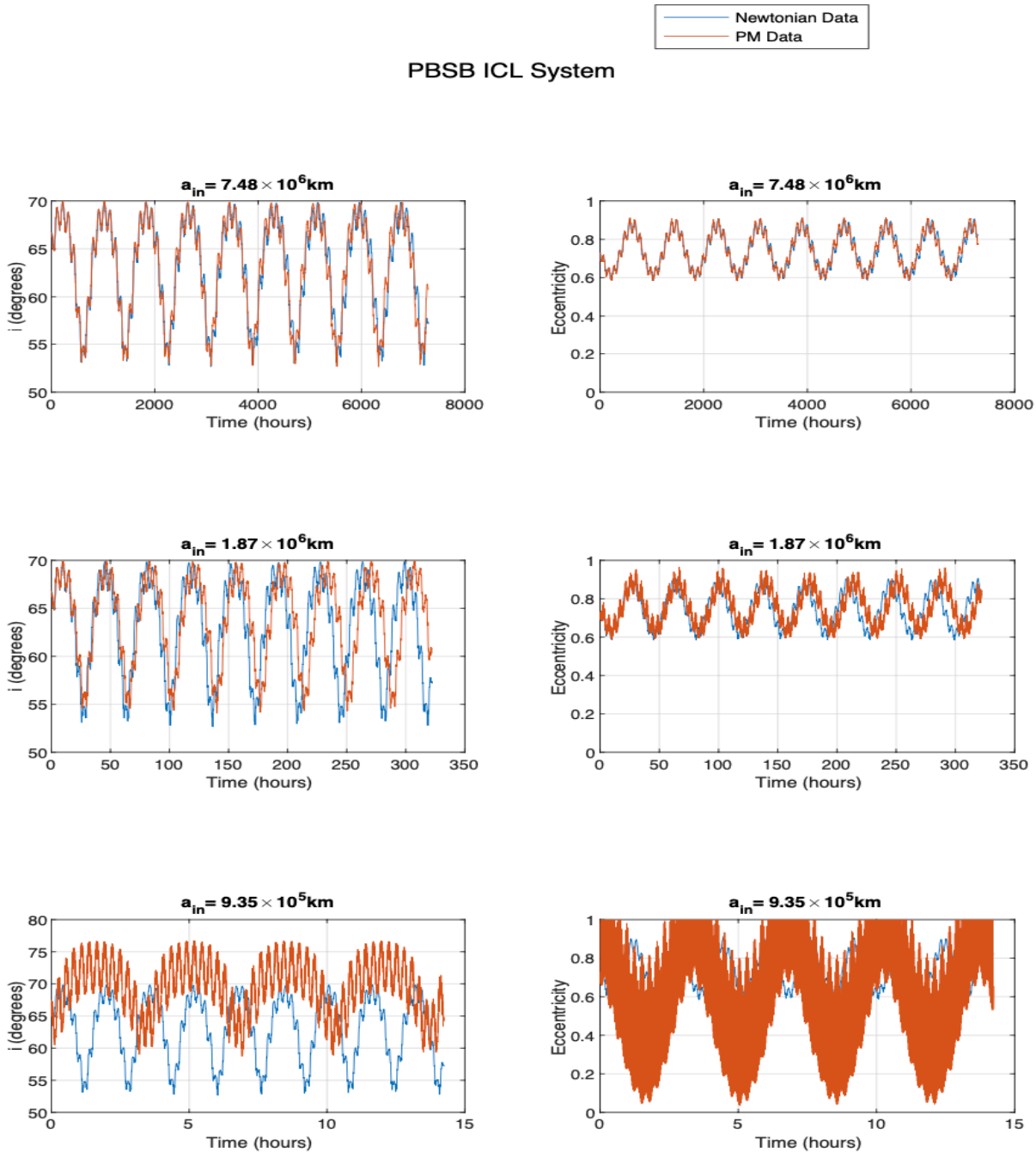

Figure B.10 Data from an initially circular system with a neutron star, a black hole, and a super-massive black hole. Initial conditions are of 'libration' type.

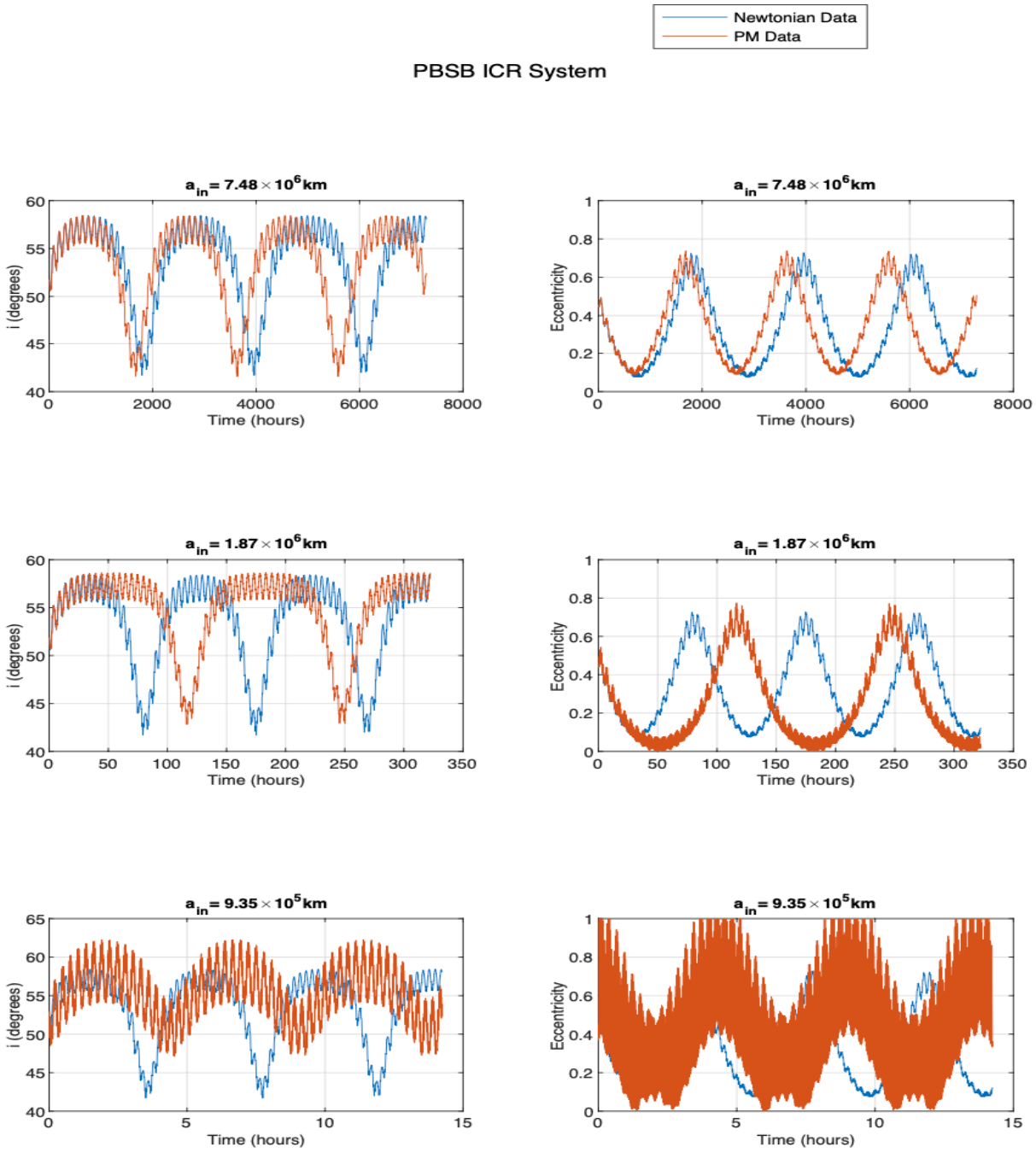

Figure B.11 Data from an initially circular system with a neutron star, a black hole, and a super-massive black hole. Initial conditions are of 'rotation' type.

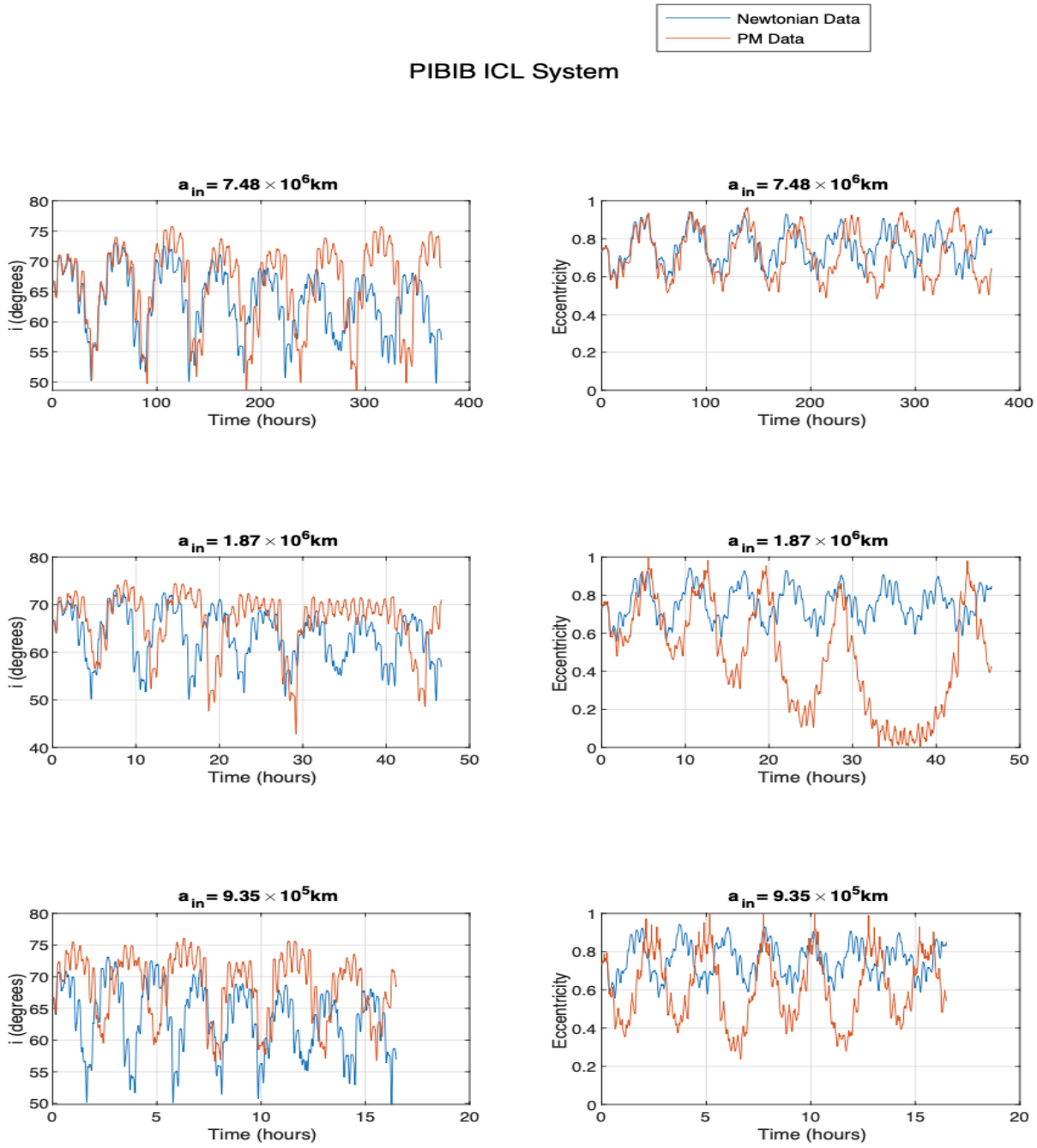

Figure B.12 Data from an initially circular system with a neutron star and two intermediate mass black holes. Initial conditions are of 'libration' type.

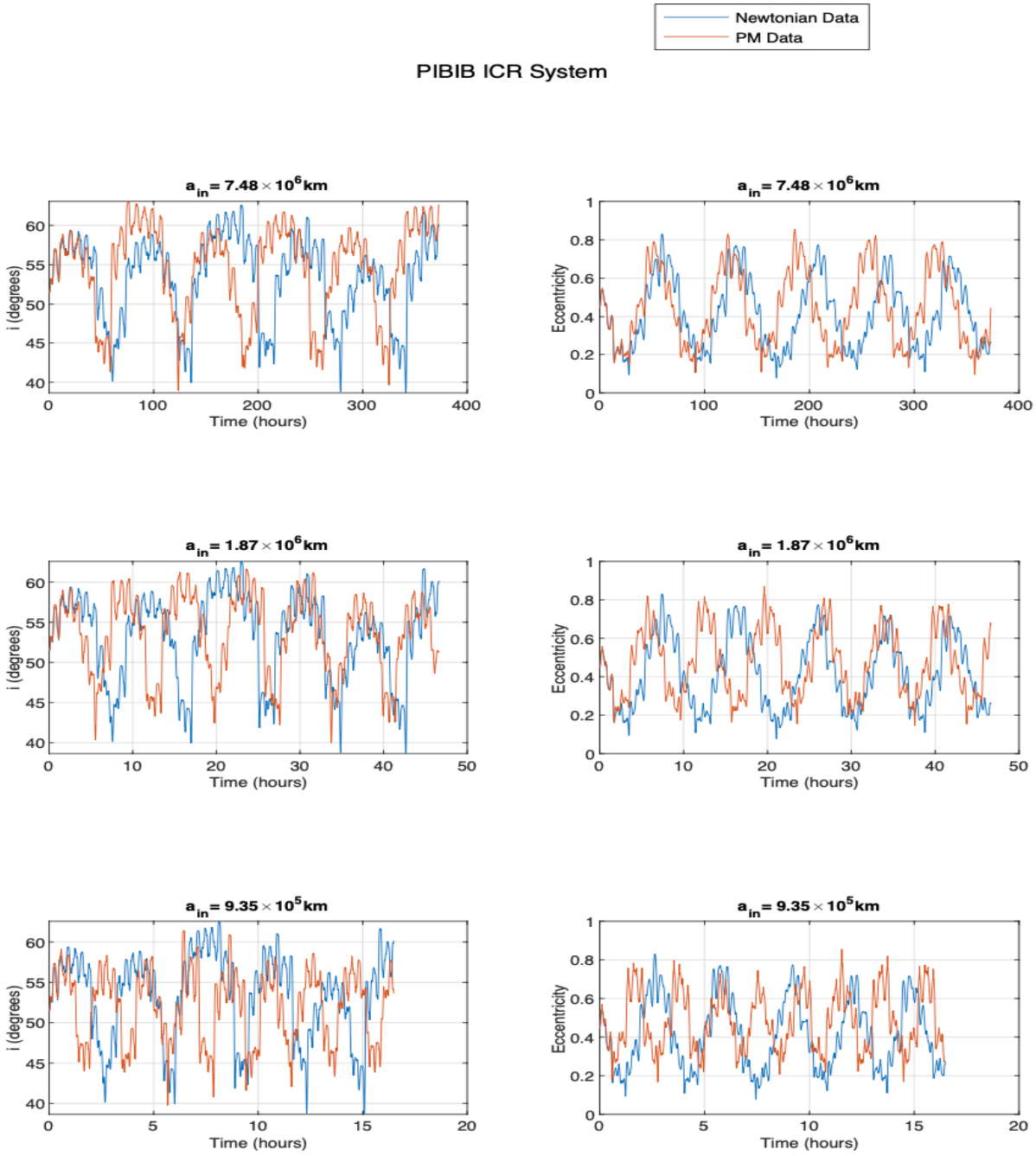

Figure B.13 Data from an initially circular system with a neutron star and two intermediate mass black holes. Initial conditions are of 'rotation' type.

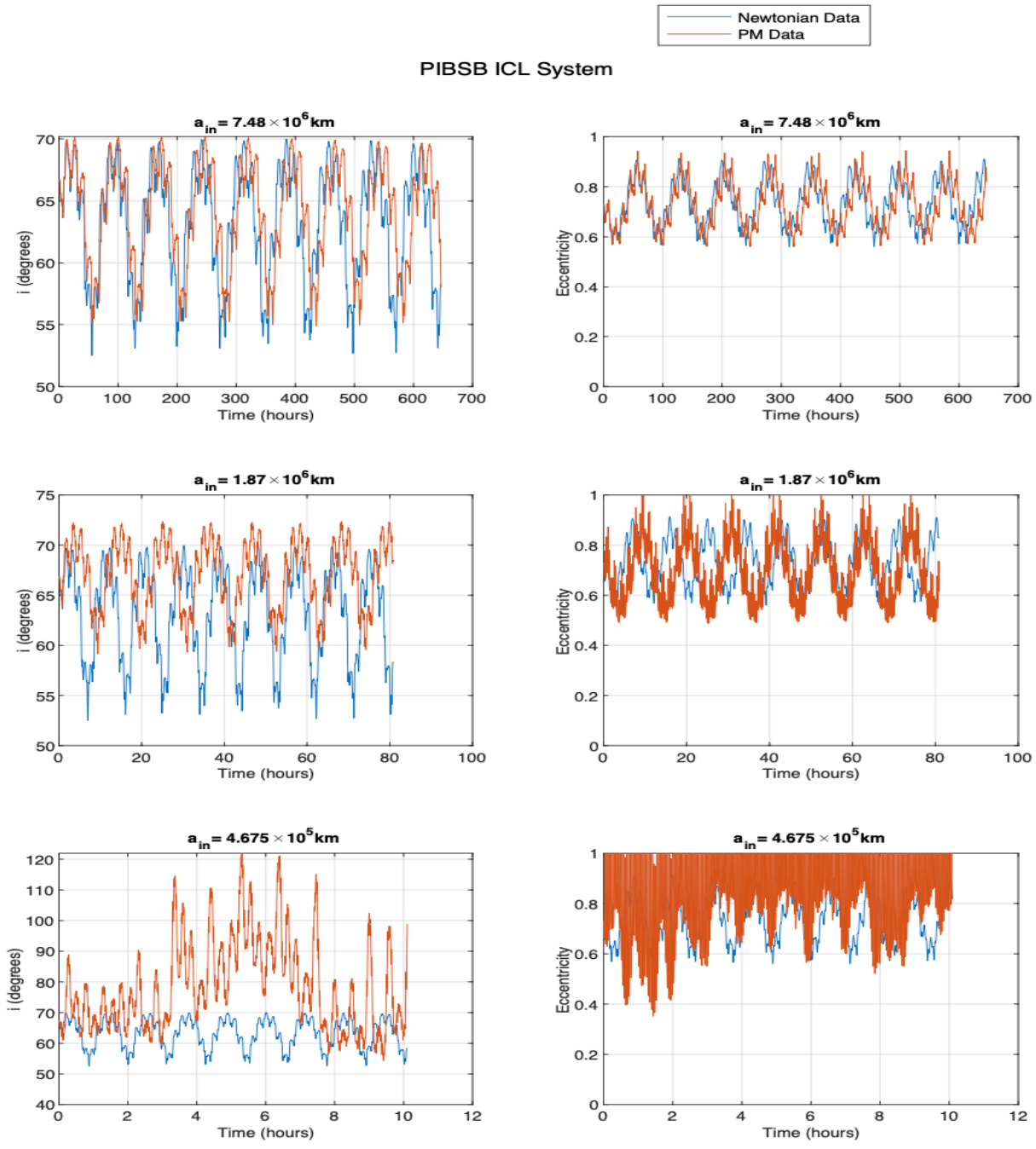

Figure B.14 Data from an initially circular system with a neutron star, an intermediate mass black hole, and a super-massive black hole. Initial conditions are of 'libration' type.

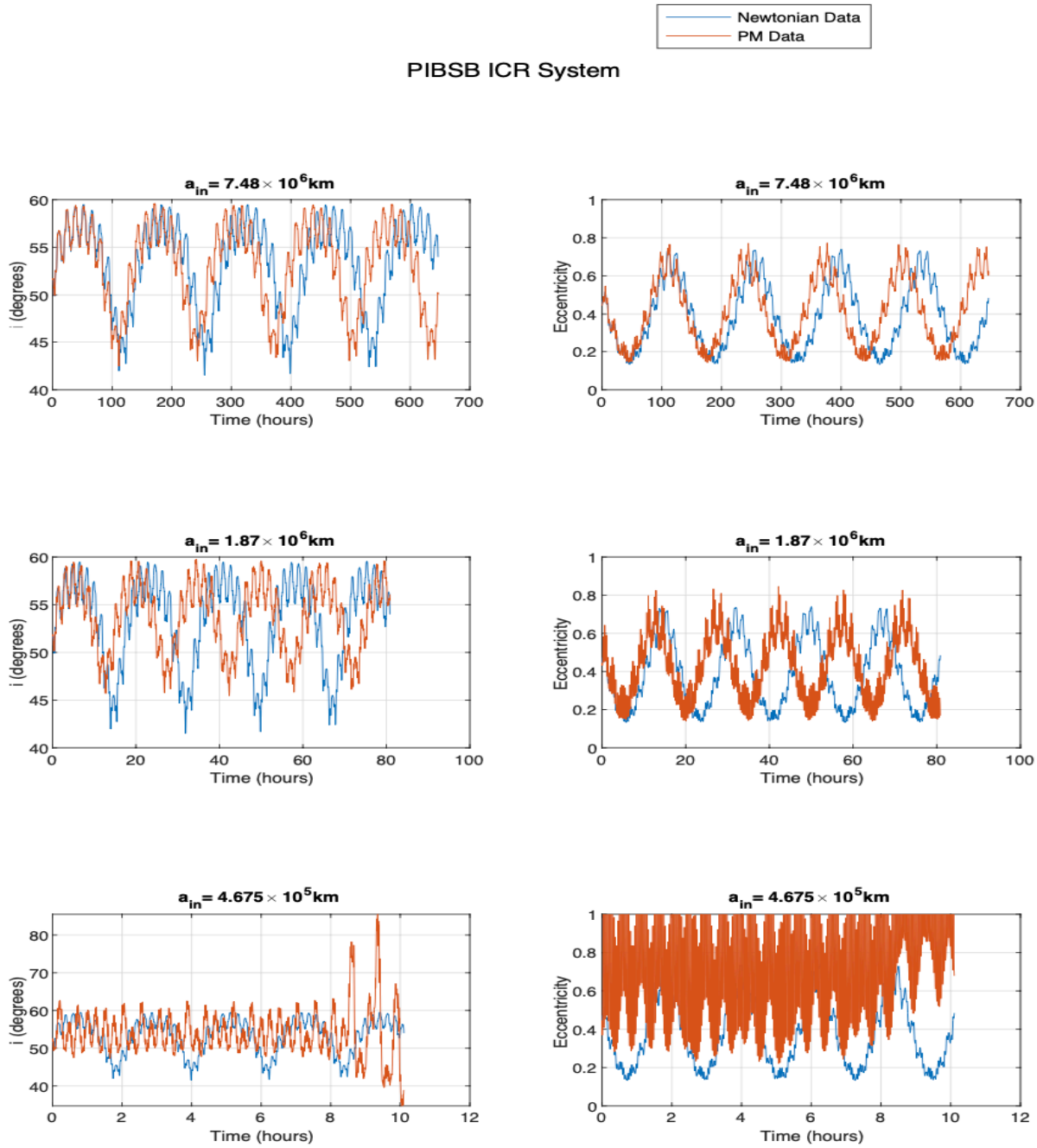

Figure B.15 Data from an initially circular system with a neutron star, an intermediate mass black hole, and a super-massive black hole. Initial conditions are of 'rotation' type.

Bibliography

Abbott, B. P., et al. 2016, Phys. Rev. Lett., 116, 061102

Antonelli, A., Buonanno, A., Steinhoff, J., Meent, M. V. D., & Vines, J. 2019, Physical Review D, 99

Bern, Z., Cheung, C., Roiban, R., Shen, C. H., Solon, M. P., & Zeng, M. 2019, Physical Review Letters, 122

Bezanson, J., Edelman, A., Karpinski, S., & Shah, V. B. 2017, SIAM review, 59, 65

Dyson, F. W., Eddington, A. S., & Davidson, C. 1920, Philosophical Transactions of the Royal Society of London. Series A, Containing Papers of a Mathematical or Physical Character, 220, 291–333

Einstein, A. 1916, Annalen Phys., 49, 769

Feng, J., Baumann, M., Hall, B., Doss, J., Spencer, L., & Matzner, R. 2018, The Astrophysical Journal, 859, 130

Geller, A. 2020, Masses in the Stellar Graveyard (LIGO-Virgo-KAGRA, Northwestern), https://media.ligo.northwestern.edu/gallery/mass-plot

Holberg, J. B. 2010, Journal for the History of Astronomy, 41, 41–64

Kraus, M. 2020, GeometricIntegrators.jl: Geometric Numerical Integration in Julia, https://github.com/JuliaGNI/GeometricIntegrators.jl

Ledvinka, T., Schaefer, G., & Bicak, J. 2008, Physical Review Letters, 100

Mardling, R. A., & Aarseth, S. J. 2001, Monthly Notices of the Royal Astronomical Society, 321, 398–420

Naoz, S. 2016, Annual Review of Astronomy and Astrophysics, 54, 441–489

Nishizawa, A., Berti, E., Klein, A., & Sesana, A. 2016, Physical Review D, 94

Oppenheimer, J. R., & Volkoff, G. M. 1939, Phys. Rev., 55, 374

Rackauckas, C., & Nie, Q. 2017, Journal of Open Research Software, 5

Suzuki, H., Gupta, P., Okawa, H., & ichi Maeda, K. 2020, Monthly Notices of the Royal Astronomical Society, 500, 1645

Will, C. M. 2011, Proceedings of the National Academy of Sciences, 108, 5938–5945

Woosley, S. E., & Heger, A. 2021, The Astrophysical Journal Letters, 912, L31

Zwart, S. F. P., Boekholt, T. C. N., Por, E., Hamers, A. S., & McMillan, S. L. W. 2021

List of Figures

List of Tables

Index